HHS Public Access

Author manuscript

ACS Appl Mater Interfaces. Author manuscript; available in PMC 2018 July 06.

Published in final edited form as:

ACS Appl Mater Interfaces. 2017 January 18; 9(2): 1189–1206. doi:10.1021/acsami.6b10568.

Mimicking Neuroligin-2 Functions in β-cells by Functionalized Nanoparticles as a Novel Approach for Antidiabetic Therapy

Anna Munder[§], **Liron L. Israel**[§,‡], **Shirin Kahremany**[§], **Rina Ben-Shabat-Binyamini**[§,‡], **Charles Zhang**[†], **Michal Kolitz-Domb**[§,‡], **Olga Viskind**[§], **Anna Levine**[ζ], **Hanoch Senderowitz**[§], **Steven Chessler**[†], **Jean-Paul Lellouche**[§,‡,*], and **Arie Gruzman**[§,*]

[§]Department of Chemistry, Faculty of Exact Sciences, Bar-Ilan University, Ramat-Gan, Israel

[‡]Nanomaterials Research Center, Institute of Nanotechnology & Advanced Materials (BINA), Bar-Ilan University, Ramat-Gan, Israel

[†]Division of Endocrinology, Diabetes & Metabolism, Department of Medicine, University of California, Irvine, California, United States

[ζ]The Scientific Equipment Center, Faculty of Biological Sciences, Bar-Ilan University, Ramat-Gan, Israel

Abstract

Both pancreatic β-cell membranes and presynaptic active zones of neurons include in their structures similar protein complexes, which are responsible for mediating the secretion of bioactive molecules. In addition, these membrane-anchored proteins regulate interactions between neurons and guide the formation and maturation of synapses. These proteins include the neuroligins (e.g., NL-2) and their binding partners, the neurexins. The insulin secretion and maturation of β-cells is known to depend on their 3-dimensional (3D) arrangement. It was also reported that both insulin secretion and the proliferation rates of β-cells increase when cells are co-cultured with clusters of NL-2. Use of full-length NL-2 or even its exocellular domain as potential β-cell functional enhancers is limited by the biostability and bioavailability issues common to all protein-based therapeutics. Thus, based on molecular modeling approaches, a short peptide with the potential ability to bind neurexins was derived from the NL-2 sequence. Here, we show that the NL-2-derived peptide conjugates onto innovative functional maghemite (γ-Fe_2O_3)-based nanoscale composite particles that enhance β-cell functions in terms of glucose-stimulated insulin secretion, and protect them under stress conditions. Recruiting the β-cells' "neuron-like" secretory machinery as a target for diabetes treatment use has never been reported before. Such nanoscale composites might therefore provide a unique starting point for designing a novel class of antidiabetic therapeutic agents that possess a unique mechanism of action.

[*]Arie Gruzman, Department of Chemistry, Faculty of Exact Sciences, Bar-Ilan University, Ramat-Gan, 52900, Israel, gruzmaa@biu.ac.il. [*]Jean-Paul Lellouche, Department of Chemistry, Faculty of Exact Sciences and Nanomaterials Research Center, Institute of Nanotechnology & Advanced Materials (BINA), Bar-Ilan University, Ramat-Gan, 52900, Israel, Jean-Paul.M.Lellouche@biu.ac.il.

Author Contributions

A.G., J-P.L., S.C. and H.S. designed the experiments; A.M., C.Z., S.K., R.B., M. K-D., O.V., A.L., S.Z., and L.I. performed the experiments; A.G., A.M., L.I., J-P.L., S.C., and H.S. co-wrote the paper.

Keywords

Neuroligin-2; Yb(III)-γ-Fe_2O_3 nanoparticles; INS-1E cells; insulin secretion; computer-aided drug design; bioactive peptides

INTRODUCTION

The loss or decreased function of β-cells, and specifically, the reduction in their insulin secretion capacity and responsiveness to glucose, play an essential role in the development and progression of type 1 and 2 diabetes (T1DM and T2DM).[1–2] T1DM pathogenesis is directly related to the lack of insulin production due to autoimmune-mediated destruction of β-cells. Despite enormous efforts to develop novel types of anti-T1DM therapies, supplying lifelong insulin is still the only effective method for treating this disease.[3] However, also in T2DM, especially in the late stages of the disease, the decreased ability of the pancreas to supply insulin (owing to β-cell damage and malfunction) significantly contributes to hyperglycemia and to the consequent development of severe diabetic complications.[4] Current treatments of T2DM have focused on improving peripheral insulin sensitivity, the inhibition of gluconeogenesis, and the stimulation of insulin secretion. However, they do not target progressive β-cell loss directly.[2] This loss leads to the lack of optimal glycaemic control in the majority of T2DM patients, and it cannot be controlled with commonly used antihyperglycaemic medications and / or insulin injections.[5–6]

Thus, a promising direction in the development of novel anti-T2DM therapies involves the protection of β-cells in order to increase or at least to preserve their mass.[7] Mass preservation could be achieved through the protecting action of small organic compounds, whereas mass increase could be achieved by the production of new β-cells. Indeed, multiple efforts have been invested in this direction over the last decade using approaches such as stem cells, β-cell proliferation, non-pancreatic cell reprogramming, among others.[8] Using this last approach, injured and non-functional β-cells of a patient are replaced by his own mature and functioning β-cells typically administered via transplantation.[9] This strategy is suitable for treating both types of diabetes.[10–11]

Intensive research is ongoing in order to elucidate the best methods for transforming human stem cells to fully differentiated β-cells for transplantation.[9–10, 12-13] Such a transformation requires a three-step differentiation process, from pluripotent stem cells to endoderm cells, from endoderm cells to pancreatic progenitors, and from pancreatic progenitors to mature β-cells. Currently these steps are hampered by low efficiency (in particular, for the second stage), expensive manufacturing costs, and great batch-to-batch variation. Moreover, even when successfully manufactured, the resulting β-cells often fail to function following transplantation. This is because in order for these cells to function properly, they need to form unique 3D cellular cluster structures (islets), which are not fully created *in vitro* prior to transplantation.[13] Thus, tissue engineering strategies may be used to provide the 3D organization of maturated β-cells required for *in vivo* functioning.[9, 14–18]

Such artificial *in vitro* self-organization of β-cells may mimic the pancreatic development and play a key role in normal insulin secretion and β-cell survival following transplantation.

In accordance with this hypothesis, it has been shown that clusters of β-cells have better physiological parameters than do single dispersed cells. [19–21] For example, such 3D cultured structures lead to β-cells with improved insulin secretion regulation in comparison with traditional two-dimensional (2D) monolayer cultures, and in addition, 3D organization of β-cells induces differentiation and the formation of islet-like structures that display greater similarities to pancreatic islets. [18, 22–23]

Although it is known that the cellular machinery of the β-cells is similar to that of neurons, there have been no systematic efforts to utilize this understanding to expedite the identification of neurosystem factors that may enhance the functionality of β-cells.[24–27] In particular, a tactic for examining the parallels between β-cell membranes and the pre-synaptic zones of neurons in order to identify molecules that mimic or enhance the beneficial effects of islet-like clustering and thereby increase insulin secretion has not been reported to date.

In this work we developed such a strategy by taking advantage of known interactions between cell surfaces, postsynaptic neuroligins (NLs), and their major binding partners, the neurexins (NXs), which are located on the neuron presynaptic membrane.[28–32] These proteins mediate interactions between neurons, and guide the differentiation, maturation, stabilization, and plasticity of both inhibitory and excitatory synapses. Furthermore, their abnormal functions were linked to several central nervous system disorders such as autism and schizophrenia. [33–36] It was shown that clustered NLs induce the formation of presynaptic zones when brought into contact with axonal membranes, and, similarly, that NXs trigger postsynaptic density formation.[37–38] In addition, in neurons, these complexes mediate the maturation of synapses with the concomitant secretion of neurotransmitters.[35] Like neurons, β-cells must be organized in 3D structures in order to function physiologically. For example, glucose-stimulated insulin secretion (GSIS) is markedly decreased when β-cells are dispersed, but this important β-cell function returns to normal when the cells are allowed to re-aggregate. [39–40]

Given the parallels between synapses and β-cells, it was suggested that specific transcellular NL and NX interactions, which are interrupted by β-cell dispersal, help establish the improved, normal β-cell functioning brought about by β-cell clustering and contact. Indeed, it was recently shown that clustered NL-2 (a member of the NL family) enhanced insulin secretion and improved pancreatic β-cell functions. [41–43] Moreover, it was demonstrated that in NL-2-deficient mice, β-cells are smaller, fewer in number, and display lower insulin content. However, insulin secretion, after normalization to content, did not decrease.[44] These results clearly indicate that NL-2 influences β-cell function and suggests that mimicking NL-2 activity *in vitro* might promote the enhanced functioning brought about in vivo by β-cell clustering., This may be useful in transplantation therapy. Based on these results, we hypothesized that clusters of NL-2 might be introduced into the diabetic pancreas locally or that β-cell precursor cells might be differentiated with clusters of NL-2 to functionalize and protect β-cells inside the body. However, using full-length NL-2 is hampered by its rapid biodegradation and the potential induction of immunogenic responses. With this in mind, a short NL-2 mimetic peptide (HSA-28: QQGEFLNYD) derived from the NL-4/NX-1 crystal complex (the crystal structure of the complex between NL-2 and NX-1 remains to be

determined) was designed, clustered, and used for inducing β-cell functions. Clustering was performed by means of conjugation onto the surface of innovative functional Yb(III) cation-doped maghemite (γ-Fe_2O_3) nanoparticles (NPs) using EDC•HCl activation/coupling (NPs COOH species activation), leading to functional nanoscale particulate composites.[45] The resulting peptide-decorated functional NPs exhibited excellent promoting biological activity in β-cells, as described here. We demonstrated that NP-clustered NL-2 mimetics enhance GSIS, protect β-cells under oxidative stress conditions, and increase their proliferation rate. The stimulatory effect of NP-clustered NL-2 mimetics on GSIS was also validated in mouse islets. Based on the observed biological activity of such functional nanocomposites, a novel type of antidiabetic therapy (β-cell protective agent and/or β-cell proliferation inducer) might be successfully developed in the near future. In addition, these NL-2 mimetics can be used for the final differentiation step in stem cell-based β-cell production *in vitro* prior to transplantation. Interestingly, Gjørlund et al. reported *in vitro* beneficial effects (inducing neurite outgrowth) of an NL-1-derived peptide, CNSP-1 (SEGNRWSNSTKGLFQRA) in neurons.[46] The peptide was also active in clusters (a tetramer coupled to a lysine backbone). Subsequently, this peptide and its modified/shortened version CNSP-2 (HSEGLFQRA) exhibited *in vivo* biological activity related to the regulation of the social behavior of mice.[47] We conjugated both peptides with Ytterbium (III) cation-doped maghemite NPs, but such NP failed to induce any biological effect on the β-cells.

Magnetically responsive maghemite (γ-Fe_2O_3)-based nanoscale particles are currently the subject of much interest due to several factors, among which is their potential use as contrast agents for *in vivo* Magnetic Resonance Imaging (MRI). In a previous work [45] , highly stable non-aggregated hydrophilic maghemite (γ-Fe_2O_3) NPs were synthesized using high-power ultrasonication of Massart magnetite (Fe_3O_4) NPs in the presence of a powerful mono electronic Ceric Ammonium Nitrate (CAN) oxidant. The resulting NPs formed a stable aqueous colloid/ferrofluid owing to a unique ultra-sound-mediated process of NP surface doping by positive $Ce^{3/4+}$ atoms/cations.

This nanofabrication methodology was extended to Ytterbium (III) cation-doped maghemite NPs, using Yb(III) perchlorate [$Yb(ClO_4)_3$] instead of CAN. [48] Doping of Yb^{+3} atoms/cations present on the NP surface, which strongly promoted colloid stabilization against NP aggregation in aqueous dispersions. Remarkably, this lanthanide cation Lewis acid-acting shell (i) provides an effective mode for attaching any organic species onto the NP surface (coordinative mode of binding), as well as (ii) strongly affects the NP T_2* MRI relaxivity feature. In addition and similarly to the previously formed $Ce^{+3/4}$ cation-doped γ-Fe_2O_3 NPs [49] the high-power ultrasonic Yb(III)-perchlorate-mediated reaction conditions led to the deposition of a polyCOOH shell onto the NP surface, providing a 2nd orthogonal potential mode for the covalent attachment of organic species (EDC•HCl activation/coupling).

RESULTS AND DISCUSSION

Owing to the lack of a crystal structure in the NL-2/NXs complex, the homologous NL-4/NX1 complex (PDB code 2WQZ; the sequence identity between hNL-2 and hNL-4 is 65.2%) was used as a starting point for designing the peptide. The interactions between NX-1 and NL-4 are mediated directly by four hydrogen bonds, namely, NX-1 Thr 235 with

NL-4 Glu361, NX-1 Pro 106 with NL-4 Asn 364, NX-1 Ser 107 with NL-4 Asn 364, NX-1 Arg 109 with NL-4 Asn 364, and by favorable VdW interactions between NX-1 Pro 106, Thr 108, Leu 234, Ile 236 and NL-4 Gly 360, Phe362, Leu 363, respectively, as shown in Figure 1A. In addition, a calcium ion indirectly coordinates with residues Asp 137, Asn 238, Val 154, and Ile 236 of NX-1 and residues Gln 359 and Gly 360 of NL-4 (Figure 1B). The only difference between the sequences of NL-4 and NL-2 at the interface with NX-1 is at position 358 (glutamate in NL-4 *vs.* glutamine in NL-2) and this mutation was manually made. Upon visual inspection of the NL-4/NX-1 interface, a nine-residue peptide (Q358-Q359-G360-E361-F362-L363-N364-Y365-D366, and HSA-28) was selected from the sequence of NL-4 as a potential binding partner of NX-1. The HSA-28 peptide was evaluated for its ability to stably interact with the NX-1 interface through MD simulations. Two independent 100 ns MD simulations were performed for the NX-1/HSA-28 system, each initiated with a different random number. Throughout both simulations, the peptide remained in proximity to the protein primarily by maintaining the coordination with the calcium ion (see Figure 2A, B). Based on the chelating distance between HSA-28 and the calcium ion, we concluded that their interaction is stable (Figure 2C). These findings therefore suggest that the designed peptide can indeed bind NX-1.

The HSA-28 peptide was synthesized with an amide moiety in its C-terminal (Chart 1) and tested in INS-1E β-cells. The analytical data related to the peptide are shown in Figure S1a. The isolated peptide did not increase the GSIS and has not shown any effect on the proliferation rate of the cells (data not shown). However, an HSA-28 dimer (HSA-112) formed by bridging two-HSA-28 monomers via amide bond formation with active ester PEG_{2000} (Scheme S1, Figure S2), dose-dependently increased GSIS in INS-1E cells (Figure 3A), with an EC_{50} of 32 μM. The effect of HSA-112 was also time dependent: after 6 hours, the compound at a 50 μM concentration induced a significant increase in insulin secretion, which lasted for 24 h. The maximal stimulatory effect of the compound was observed after 18 h and consisted of a twofold elevation of GSIS parameters (Fig. 3B). HSA-112 did not affect the cellular insulin content (data not shown). In addition, HSA-112 exhibited a cytoprotective effect on glucose oxidase-induced oxidative stress. The effect of the compound on cell viability was almost identical to that of the well-known antioxidant (trolox), which was used as a positive control (Fig. 3C). Since HSA-112 did not seem to be an antioxidant, we hypothesized that cell protection resulted from the ability of the compound to induce β-cell clusters, which are much more resistant to any kind of damage including oxidative stress, than are dispersed cells.[39] Simple cell counting revealed that indeed the amount of cells in the presence of HSA-112 was higher than that in the control dishes (Fig. 3D). Despite the good biological activity of HSA-112, its *in vitro* active concentration, 50 μM, might be too high for further development of *in vivo* active molecules. In addition, the lack of an effect on the insulin content was an additional source of concern. Having observed a positive effect of HSA-28 upon dimerization via the PEG linker, a poly-HSA-28 cluster was generated by covalent linking the peptide onto the maghemite-based NP surface *via* its *N*-terminus (Scheme 1). Consequently and similarly to the formerly described $Ce^{3/4+}$-cation-doped γ-Fe_2O_3 NPs , pre-formed Massart[50] magnetite NPs were reacted with Yb(III)-perchlorate [$Yb(ClO_4)_3$] in an inert argon atmosphere using a high power Ti horn probe sonicator to produce corresponding Yb^{3+} cation-doped maghemite (γ-Fe_2O_3) NPs

functionalized by a polycarboxylic acid (polyCOOH) shell.[48, 50] Selected significant characterization data have been gathered, as shown in Figures 4–6. A TEM microphotograph (Fig. 4A) was combined with a SAED X-ray (Fig. 4B) diffraction pattern and confirmed the crystallinity of Yb^{3+} cation-doped γ-Fe_2O_3 NPs while providing an average 6.58 ± 2.03 nm-sized NP diameter (NP TEM size histogram, Fig. 4C). An XRD spectrum (Fig. 4D) of the NP surface doping by Yb(III) cations/complexes (perchlorate coordinated ligands, *elemental Yb presence)* has been confirmed by elemental TEM-EDAXS (Yb(III) L: 1.92 atomic %, and ICP-AES (Jobin Yvon Ultima 2, see the complete quantitative data in Table 1 below). Moreover, elemental Yb could not be directly detected by surface-sensitive XPS due to its low level of NP doping. However, this same NP surface analysis method enabled easy detection of both (i) Yb(III)-coordinating perchlorate ligands (Fig. 4E&F, XPS, Cl_{2s} & Cl_{2p} peaks: binding energies of 278.530 & 208.230 eV, respectively), and of (ii) the organic ultrasound-generated polyCOOH shell (Fig. 4G, XPS, C_{1s} (polyCOOH functional shell): binding energy of 288.991 eV). Quantitative confirmation of the presence of this organic polyCOOH functional shell has been further obtained by using a differential sensitive ninhydrin-based UV spectrophotometric Kaiser test [51] with coupling of 1,4-diaminobutane in excess *with* and *without* polyCOOH activation by EDC•HCl carbodiimide.[49] This measurement provided a 0.129 mmol concentration of COOH groups (polyCOOH shell)/g on the surface of the NPs, which is useful for variable underlayer/uplayer 2nd step quantitative ligand attachment onto the NP surface. Yb^{3+} cation-doped γ-Fe_2O_3 NPs have also been characterized by SQUID magnetization profile analysis at 298°K (Fig. 4H), demonstrating no hysteresis, as expected for super-paramagnetic NPs and a saturation magnetization value, *Ms*, of 70.4 emu/g NPs.

In a 2nd step of NP covalent decoration, the HSA-28 peptide was covalently conjugated onto the surface of functional Yb(III)-doped γ-Fe_2O_3 NPs *via N*-terminus amide bonding using EDC•HCl carbodiimide polyCOOH shell activation/coupling, leading to functional nanoscale composites of the peptide (Scheme 1). The final concentration of the peptide was determined by HPLC, as shown in Figure S3. For HSA-28P the concertation of the conjugated peptide was 0.988 mM and for HSA-28P1/2 it was 0.494 mM, respectively.

For this purpose, two different quantities of EDC•HCl conjugated peptide were used, based on the former Kaiser polyCOOH shell quantification, *i.e.,* 100% (1.0 eq *vs.* NPs surface COOH quantity, 1.1 mg HSA-28 peptide, 0.988 μmol) and 50% (0.5 eq *vs.* NPs surface COOH quantity, 0.55 mg, 0.494 μmol) of the total quantity of carboxylic acids (polyCOOH shell) present on the NP surface. The TEM microphotographs (100% COOH functions for peptide attachment) and the TEM-derived size distribution (7.86±2.18 nm) of the resulting functional peptide-decorated NPs (f-NPs) are reported in Figure 5. In addition, thermogravimetric TGA analyses were performed (Figure 6A), and revealed total weight losses of both peptide-conjugated f-NPs in comparison with core Yb(III)-γ-Fe_2O_3 NPs (Figure 6B). Such weight losses (core Yb(III)-γ-Fe_2O_3, 13.85% - T°C range: 94.28–253.15°C; 50% f-NPs, 10.05% - T°C range: 91.62–477.37°C; 100% f-NPs, 8.8352% - T°C range: 91.55–477.19°C) mainly accounted for HSA-28 peptide covalent attachment. Note that the covalent attachment of approximately 50% and 100% peptide to the functionalized NPs most likely led to the removal of weight-increasing polyCOOH organic layer components from the f-NPs surface, thus providing a plausible explanation as to why TGA

analyses were unable to quantify the exact quantities of linked peptide onto the surface of respective f-NPs. In order to further track the effective peptide covalent attachment, both DLS and ζ potential measurements were also performed. Whereas core Yb(III)-γ-Fe_2O_3 NPs displayed a DLS value of 42.0 nm and a highly positive ζ potential in the +46-+50 mV range, both 100% and 50% peptide-conjugated-f-NPs displayed higher average DLS hydrodynamic diameter values in the micrometer range (2,062 and 2,357 nm, respectively) as well as negative ζ potential values (−15.1 and −16.0 mV, respectively).

Similar to the original peptide, the biological evaluation of HSA-28P was also performed in a rat INS-1E cell line. HSA-28P dose- and time-dependently enhanced GSIS was compared with untreated cells and control cells treated with the “naked” NPs and by identical NPs covered by a “scrambled” peptide (Figure 7 A&B). The analytical data of “scrambled” peptide are shown in Figure S1b. The maximal stimulatory effect on GSIS was obtained after 18–24 h of incubation at a concentration of 3 μM/μg of NPs/ml. Importantly, the stimulatory effect on GSIS was significant already at a concentration of 0.6 μM/per μg NPs/ml of HSA-28P. The total insulin content was also significantly elevated by HSA-28P in both (low and high) glucose concentrations after 24 h of incubation (Figure 7C). The effect of HSA-28P on INS-1E β-cells’ viability under oxidative stress conditions (glucose oxidase/glucose system) was further investigated. After 24 h INS-1E cells that were placed in plates together with HSA-28P (3 μM/ per μg of NPs/ml) exhibited higher viability (dose response behavior) than all the tested controls did (see Figure 7D). This cell protective effect was equal to the effect that was induced by trolox. Finally, the number of cells was also significantly higher in HSA-28P-treated samples compared with the control (Figure 7E). Likewise, the effect of the compound on the cell number was dose dependent. We suppose that the compound induced the formation of β-cell clusters, as shown in Figure 7F&G, as a result of the increased proliferative rate. The possible proliferative stimulation of non-β-cells by HSA-28P was also investigated. Two types of cells, PC-3 (human prostate cancer cells) and PC-12 cells (rat pheochromocytoma) were chosen for this control experiment. No significant effect of HSA-28P was observed in PC-3 cells, yet similarly to its effect on β-cells, HSA-28P increased the proliferation of PC-12 cells approximately by 40% (Figure S4). Such results are not surprising due to the presence of neuroligins and neuroxins in the plasma membrane of neuronal PC-12 cells.[52] These data indicate that the ability of HSA-28P to stimulate cell growth is specific to cells that were developed from the ectodermal/endodermal precursor population common to neurons and β-cells.

According to our hypothesis, NPs decorated with HSA-28 should interact with NXs that are located on the plasma membrane of the INS-1E cells and thereby induce formation of functional NX clusters on the β-cell surface. To test this hypothesis, FITC-labeled HSA-28 NPs were fabricated. A commercially available lysine (protected in its amine terminal by a 4-methyltrityl group) was conjugated with the last amino acid in the sequences of HSA-28. After the removal of the protective group, the free primary amine was reacted with FITC-isothiocyanate isomer I. Next, the labeled peptide was cleaved from the resin and used for the coupling with core Yb(III)-doped maghemite NPs, as described above. However, this composite led to a very weak intensity of the fluorescent signal and consequently we decided to directly label the NPs by the same FITC dye. In order not to drastically affect the NPs’ surface (core Yb(III)-maghemite NPs for control and HSA-28P f-NPs), labeling was

performed via a simple adsorption technique. HSA-28P and control core NPs (Yb(III)-maghemite NPs; 1.5 mL aqueous dispersion, Fe = 1.45 mg/mL, a total Fe amount of 2.175 mg) were treated with 2.73 mg of FITC (fluorescein isothiocyanate, 7.01 μmol) in 5 mL of milliQ-purified H_2O and the mixture was shaken for 2 hours at room temperature (60° rotation angle, 80 rpm). Excess FITC was removed by centrifugation-mediated washings (3 × 10 mL ddH_2O) using an Amicon® Ultra-15 centrifugal filter device (100K) operated at 4,000 rpm (5 min), followed by a 2 cycles of gravitational centrifugation (4,000 rpm/min, 6 min, 15°C). Cleaned and labeled NPs were finally dispersed in 4 mL of H_2O (Fe = 0.157 mg/mL). For both HSA-28P f-NPs, 3 mL of each peptide-conjugated f-NP aqueous suspension (Fe = 0.241 mg/mL, total Fe amount of 0.723mg) were brought in contact with 4.71 mg FITC (12.1 μmol). Each mixture was then shaken overnight (200 rpm) at 14.5°C and excess FITC was washed with milliQ-purified H_2O (4×10 mL) using centrifugation-NP precipitation (4 cycles, 4,000 rpm, 5 min, 15°C). The resulting cleaned FITC-labeled fluorescent f-NPs were then re-dispersed in 2.5 mL of H_2O (Fe = 0.0724 mg/mL).

FITC-labeled HSA-28P f-NPs were added to INS-1E cells for 24 h, washed, and then assessed by fluorescent microscopy. As shown in Figure 8A, the number of cells present after treatment with control NPs was significantly less than the number after treatment with HSA-28P labeled NPs (Figure 8A'). A significant difference in the fluorescent signal was also obtained (see Figure 8 B&B'). However, to rule out the possibility that the differences in the fluorescent signal are only related to the absolute obvious changes in the number of cells, zoomed-in pictures were taken (Figure 8 a,a',b,b'). These pictures show approximately identical amounts of confluent cells in both treatment groups, although with significant differences in the fluorescent signals. The fluorescent intensity of both treated and untreated cells is summarized in Figure 8C. Importantly, the fluorescent signal is selectively associated with the cells and was not detected in the medium.

The plasma membrane of β-cells was hypothesized to be the primary target for NL-2 mimetics. Thus, the association of the NPs with the plasma membrane of INS-1E was investigated. To this end, INS-1E cells were grown on cover slips, and then incubated with HSA-28P (Fe concentration, 0.0035 mg/ml) for 24 h. After fixation, phalloidin staining was used to mark the plasma membrane and DAPI was applied to indicate the cells' nuclei. The resulting slides were subjected to confocal microscopy. FITC-labeled HSA-28P f-NPs were localized solely on the plasma membrane (Figure 9A), in contrast with cells treated by "naked" FITC-labeled NPs (Figure 9B). Weak fluorescent signals were observed in "naked" FITC-labeled NP cells in comparison with strong signals in cells treated by HSA-28P. These data indicate that either HSA-28P interacts very strong with the plasma membrane or maybe enter to cytosol because even after massive washing procedure (2 washes of live cells with medium and a total of 16 washes of fixed cells with PBS) did not affect the strong fluorescent signal of HSA-28P. Moreover, the control NPs, lacking specific NL-2 interactions, were easily washed out.

The positive effect of HSA-28P on the rate of insulin secretion and the insulin intracellular content was further demonstrated by an immunocytochemistry-based assay, namely, the determination of the intracellular accumulation of C-peptide. This small peptide links between two chains of insulin and assists in processing mature insulin inside the

endoplasmic reticulum. Importantly, the ratio between C-peptide and insulin is equal in secretory granules of β-cells and both proteins are secreted simultaneously in blood circulation. Thus, the measurement of C-peptide is an indirect, but a very precise method for determining insulin synthesis and storage. In contrast, direct measurement of insulin can be problematic because, in addition to endogenous insulin that β-cells produce, the insulin from the serum of growth medium is also able to bind to the primary antibody. In contrast, the primary antibody against C-peptide is selective only to one specific species (in our case rat β-cells) and in the added serum C-peptide is not present. INS-1E cells were treated as described above. The plasma membrane and nuclei were marked similarly. Slides were exposed to a primary antibody against C-peptide and after incubation and substantial washing the secondary antibody (goat-anti-rabbit IgG labeled by ALEXA Fluor 488 nm) were added. The cells were tested by confocal microscopy. Cells treated by HSA-28P expressed significantly more C-peptide (approximately 3-fold) than did the control ("naked" NPs), which did not affect the basal level of the C-peptide (Figure 10). We normalized the intensity of the C-peptide level by the intensity of the membrane signal. These data are consistent with the results that we obtained regarding the stimulatory effect of the compound on the insulin secretion and storage, as shown in Figure 7A-C. Although the effect of HSA-28P on the insulin content was not as dramatic as its effect on the C-peptide accumulation, the positive correlation between these two effects suggests that the test compound indeed increases insulin production and secretion.

Sometimes, an increased proliferation rate of β-cell lines leads to a decrease in their differentiation level.[53] This can be observed by abnormally elevated levels of other hormones, for example, the production and secretion of glucagon (the functional antagonist of insulin).[54]Although the INS-1E cell line is the most commonly used in vitro model for studying β-cell functions), it is not an exclusively insulin-producing β-cell line, since basal levels of glucagon are still produced and secreted by these cells.[55] Thus, the possible effect of HSA-28P on the level of glucagon was investigated (Figure 11). Neither 'naked" NPs nor HSA-28P affected the level of glucagon expression. These data support our conclusion that HSA-28P stimulates cell proliferation, insulin production, and secretion without significantly influencing the differentiated phenotype of the β-cells.

In order to prove that the biological activity of HSA-28P related to the binding of NL-2 to NX-1, the flow cytometry experiment was conducted. The cells were treated with HSA-28P([Fe]-0.0035 mg/ml, [HSA-28]-3 μM), "naked nanoparticles ([Fe]-0.0035 mg/ml]) and HSA-28 (3 μM) for 24 h. The cultures were exposed to ATTO 488 labeled antibody against an extracellular epitope of NX-1α. As shown in Figure 12 the treatment by HSA-28P and by the HSA-28 peptide significantly reduced the fluorescent signal. HSA-28P and HSA-28 decreased the antibody binding by 44.1 % and by 52.8% respectively. This data likely might be explained by the fact, that (as we proposed in our working hypothesis) both mimicking NL-2 compounds bind to NX-1 and compete with the antibody for the interaction site on NX-1.

INS-1E is an immortalized cell line and may not entirely reflect the function of primary β-cells within Langerhans islets.[56] Islets consist of a heterogeneous population of endocrine cells, including insulin-producing β-cells (approx. 65–70%), glucagon-secreting α-cells

(20–25%), somatostatin-secreting δ-cells, polypeptide (PP)-secreting cells, and ε-cells producing the hormone ghrelin. The cellular and biochemical mechanisms by which glucose stimulates insulin secretion by pancreatic β-cells can be studied using islets isolated from rodents. Rat and mouse islets serve as an ideal source of insulin-producing tissue to study pancreatic β-cell function, and it is possible to obtain 300–600 islets/rat or 80–180 islets/mouse from a single pancreas. The method used to isolate pancreatic islets is based on the protocol originally developed by Lacy and Kostianovsky with some modifications.[57] We also studied the effect of HSA-28P on GSIS in freshly isolated mouse islets. It was found that HSA-28P significantly increases insulin secretion in a dose-dependent manner (Figure 13A&B). The maximal effect was observed at a concentration of 0.39 μg/ml (around a twofold stimulatory effect). In addition, two types of NPs, which were covered by CNS active NL-1 peptides, were tested. Both NPs (CNSP1 covered by SEGNRWSNSTKGLFQRA (Figure S1c) sequences and CNSP2 covered by HSEGLFQRA (Figure S1d) sequences) were unable to increase the GSIS in isolated islets. In contrast, L-arginine, which served as a positive control, significantly raised GSIS in isolated mouse islets (Figure 13B). The small but significant effect on the insulin content was obtained upon treatment of isolated mouse islets by HSA-28P using both tested concentrations (Figure 13C).

CONCLUSIONS

In summary, we have shown that the activation of the NL-2 pathway represents a novel strategy for regulating pancreatic β-cell numbers and functional maturity. Use of the neuron machinery present in β-cells in a “frozen” form due to their embryonal source for the secretion of mediators was never reported before. Starting with a computational work, a single NL-2-derived peptide was chosen for *in vitro* evaluation. Presenting multiple copies of this peptide on the surface of nanoparticles to β-cells increases insulin secretion, leads to the proliferation of insulin-containing β-cells, and protects cells against oxidative stress. The positive effect of HSA-28P was also obtained in isolated mouse islets, which makes the approach presented in our study physiologically relevant. Moreover, the use of the NL-2-based clusters may support the differentiation and maturation of human embryonic stem cells derived from pancreatic progenitors. Work towards the development of potential antidiabetic drugs and β-cell protective strategies is currently ongoing in our laboratories.

MATERIALS

The following reagents were purchased from Sigma-Aldrich Chemicals (Rehovot, Israel): L-arginine, benzophenone, collagenase Type XI, ceric ammonium nitrate (**CAN**, $Ce^{IV}(NH_4)_2(NO_3)_6$, DAPI, DIC, 3-(4,5-dimethythiazol-2-yl)-2,5-diphenyl tetrasodium bromide, EDC•HCl carbodiimide, Ficoll type 400 DL, $FeCl_3$•$6H_2O$, $FeCl_2$•$4H_2O$, FITC, glucose oxidase, 1,4-diaminobutane, D-glucose, 10x HBSS without bicarbonate and phenol red, HCl,1M HEPES pH 7.4, IGEPAL, KRBB, MT reagent, NH_4OH (ACS reagent, 28–30%), ninhydrine, 10x PBS solution, piperidine, PMSF, PEG_{2000}, polylysine, protease inhibitor cocktail, 7.5% sodium bicarbonate solution, RIPA buffer, sodium orthovanadate, sodium-β-glycerophosphate, sodium pyrophosphate, $Yb(ClO_4)_3$. DMAP and sodium fluoride were obtained from Merck (Whitehouse Station, NJ). Linco Research Inc. (St.

Charles, MO) provided the ^{125}I-labeled insulin. FCS, L-glutamine, DMEM, Trypan blue, RPMI-1640, and antibiotics were purchased from Biological Industries (Beth-Haemek, Israel). Sodium hydroxide and formaldehyde (4% in PBS) were purchased from Bio-Lab., Jerusalem, Israel. Apollo Scientific Limited (Manchester, UK) supplied BSA. HMBA-AM resin, BOP, HOBT, DIEA, protected amino acids, and succinic anhydride were obtained from Chem Impex (Wood Dale, IL, USA). β-Mercaptoethanol was purchased from Bio-Rad (Hercules, CA, USA). Alfa Aesar (Ward Hill, MA, USA) supplied t-isopropanol-silane. Alexa Fluor 633 Phalloidin was purchased from Life Technologies, Carlsbad, CA, USA). Anti-Neurexin 1α (extracellular)-ATTO-488 antibody was purchased from (Alomone Labs, Jerusalem, Israel). Synthetic nutrient 199 medium was obtained from Biotest laboratory (Ottawa, Canada). Anti-glucagon, anti-C-peptide antibody, and glucagon were supplied by Abcam (Cambridge, MA, USA). All organic solvents were purchased from Carlo Erba Reagents (Val De Reuil, France). Dry THF was obtained by reflux on sodium wire in the presence of benzophenone. Pyridine was dried with pellets of KOH. Analytical and preparative HPLC (Young Lin Instruments, Anyang, Korea) were performed on LUNA C18 preparative (10 μm, 100 × 30 mm) or analytical (5 μm, 250 × 4.6 mm) columns, both from Phenomenex, Inc. (Torrance, CA). HPLC purification was performed using an increasing linear gradient of acetonitrile in water. Analytical TLC was carried out on pre-coated Silica gel 60F254 (Merck) sheets using UV absorption and iodine physical adsorption for visualization. Organic solvents (HPLC grade) were from Frutarom Ltd. (Haifa, Israel). Dry THF was obtained using distillation from a boiled blue color mix with sodium/ benzophenone. Mass spectra were recorded on a Finnigan Model 400 mass spectrometer, using a QToF micro spectrometer (Micromass, Milford, MA) using electrospray ionization (ESI) and MALDI-TOF mass spectrometer (Bruker, Germany) in positive ion reflector mode. Flow cytometry analysis was performed using Gallios Fluorescence Activated Cell Sorter (Beckman Coulter Life Sciences, USA). Data were processed using mass LynX v.4.1 calculation and de-convolution software (Waters Corporation, Milford, MA).

The average size and shape of the fabricated NPs were measured using a JEOL transmission microscopy instrument (JEM 2100, JEOL USA, Inc., 200 kV acceleration voltage) equipped with a CCD 4×4k camera (Gatan). TEM samples were prepared by placing a drop of each aqueous NP dispersion (200–250 μg/mL) onto 400-mesh carbon-covered copper TEM grids (400C-FC, Electron Microscopy Sciences, Hatfield, PA, USA), followed by drying in a vacuum chamber at ambient temperature. Hydrodynamic size (DLS, dynamic light scattering) and surface charge (ζ potential, NPs electrophoretic mobility) of NPs (aqueous dispersions) were determined using a ZetaSizer Nano-ZS (Malvern Instruments Ltd, Worcestershire, UK - 633 nm He-Ne laser & DTS1060C-Cleare disposable zeta cells). The amounts of elemental Yb and Fe metal ions were quantified using an ICP-AES (Inductively coupled plasma atomic emission spectroscopy) ULTIMA 2 spectrometer (HORIBA, Jobin Yvon, Inc.) after sample dissolution in concentrated HCl (≈ 0.5 mL) at ambient temperature and ddH_2O dilution (volumetric flask). Sample filtration (Nylon Milipore filter, 0.22 μm) was performed prior to any ICP measurement in parallel with instrumentation calibration using standard acidic solutions of elemental Yb and Fe.

Thermogravimetric analyses (TGA) were obtained using a TGA/DSC1 analyzer (Mettler-Toledo, OH, USA) for which dry NPs samples (3–5 mg) were taken. Thermograms were recorded under nitrogen at a heating rate of 10°C/min^{-1} over a 25–800°C temperature range. Surface elemental analyses were acquired by X-ray photoelectron spectroscopy (XPS) (model AXISHS, Kratos Analytical, UK) using AlK lines at 10^{-9} Torr with a take-off angle of 90°. Saturation magnetizations M_s and coercivity factors, H_c, were measured using a SQUID magnetometer (Quantum Design, MPMS XL model) operating in a 2 to 400°K temperature range with magnetic fields up to 5.5T.

METHODS

Protein preparation for molecular modeling

Prior to molecular dynamics (MD) simulations, the peptide was capped by an amide group in its C-terminus in accordance with the anticipated peptide synthesis procedure and both the protein (NX-1) and the peptide (HSA-28) were prepared using the Prepare Protein protocol in Discovery studio version 2.5.[58] This protocol inserts missing atoms in incomplete residues, models missing loop regions, and sets the protonation state of titratable residues based on predicted pKa values.

MD simulations

MD simulations were performed using the Gromacs Molecular Dynamics package[59] (version 4.5) with the AMBER99SB-ILDN force field.[60] The system (a protein and peptide) was submerged in TIP4P water in a dodecahedral box with an extra extension along each axis of a peptide of 10Å. Ions were added to the solution to make the system electrically neutral. The structure was minimized, equilibrated (first under NVT conditions for 100 ps and then under NPT conditions for an additional 100 ps) and finally simulated under NPT conditions for 100 ns. The simulations were performed at 300°K with a time step of 2 fs using the leap-frog algorithm.[61] The cutoff for van der Waals and Coulomb interactions was set to 10 Å. Long-range electrostatic interactions were computed using Particle Mesh Ewald Summation.[62] Periodic boundary conditions were applied. The LINCS algorithm.[63] was used to constrain the bond lengths. The production phase was performed twice, each time starting from a different random number.

Peptide synthesis

Three peptides were synthesized (QQGEFLNYD, SEGNRWSNSTKGLFQRA, and HSEGLFQRA) using a solid phase method. Briefly, the synthesis was performed using 0.5 mmol Rink amide resin (0.52 mmol/g loading). The resin was loaded with the first AA (10 eq) using TBTU (80 mg/2.5 mmol) / DIEA (32mg/2.5 mmol) chemistry. Coupling completion was checked by UV absorption at 299 nm. Fmoc protecting groups were removed by treatment with a 20% piperidine/DMF solution. The remaining AA (4.5eq) was coupled using TBTU (80 mg/2.5 mmol), and DIEA (32mg/2.5 mmol). Ninhydrine tests were performed after each coupling. Cleavage of the crude peptide and deprotection of the Trt and OtBu protecting group was carried out using a solution of 95% TFA, 2.5% t-isopropanol-silane, and 2.5% H_2O.

Synthesis of HSA-112

First, 0.4 g (0.2 mmol) of PEG_{2000} was dried by three cycles of toluene washes with subsequent evaporation. The dry PEG_{2000} was reacted with 0.04 g of succinic anhydride (0.4 mmol) in 10 ml of dry tetrahydrofurane (THF) and 0.3 ml of dry pyridine under a nitrogen atmosphere at 60^0 C. The reaction mixture was left stirring for 24h. After the removal of THF under reduced pressure, the product PEG_{2000}- succinic acid was repetitively precipitated and washed with a large volume of diethyl ether. Next, the purified PEG_{2000}-succinic acid was dissolved in 20 ml of dry THF, followed by the addition of 0.04 g (0.4 mmol) of NHS (0.17gr), and then 0.08 g of DCC (0.4 mmol). The resulting mixture was stirred for 8 h at room temperature before the removal of insoluble materials. Then the NHS-ester of PEG_{2000}-succinic acid was repetitively precipitated and washed with a large volume of diethyl ether, and the product was dissolved in dioxane. This solution was added to a solution of HSA-28 that was dissolved in $NaHCO_3$ 15% in dioxane in a 1:1 ratio. The mixture was stirred at room temperature for 48 hours. The solution was filtered and the solvent water and dioxane were removed. The remaining white powder was dissolved in 30 ml of hot EtOH/CH_2Cl_2 and was filtered again and evaporated. The solid residue was dissolved in hot EtOH/ether solution (5ml), and left overnight at 4^oC. The white precipitate was filtered and further purified by HPLC, using a stepwise gradient of water and acetonitrile, and white crystals were obtained.

Synthesis and characterization of NPs

Yb(III)-doped maghemite (γ-Fe_2O_3) NPs—A 20 mL aliquot was taken from the neutral MASSART magnetite NP aqueous suspension prepared according to Massart et al., and ytterbium perchlorate ($Yb(ClO_4)_3$, 50% wt in ddH_2O, 0.475 mL, 0.742 mmol) was added rapidly to the NPs under an inert N_2 atmosphere followed by additional degassed ddH_2O (4.0 mL). Subsequently, analytical grade MeCOMe (4.0 mL) was added, and the mixture was sonicated (1h, 0°C) under an inert argon atmosphere using a high-power sonicator (Sonics®, Vibra cell, 750 Watt, power modulator set at 25%) equipped with a Ti horn. The resulting Yb(III)-doped maghemite (γ-Fe_2O_3) NPs were washed with water (3 × 10 mL) using an Amicon® Ultra-15 centrifugal filter device (100K), at 4,000 rpm, 5–6 min, and re-dispersed in ddH_2O (10 mL). Subsequently, cleaned NPs were centrifuged in a regular tube (10 min, 8,000 rpm) to eliminate micrometer-sized aggregates, whereas the corresponding supernatant phase containing the dispersed cleaned non-aggregated NPs was retained.

Both NP organic shell (polyCOOH shell) derivatizations (coordination/contacting mode – *the absence of* activating EDC•HCl, & organic shell activation using EDC•HCl), together with UV spectroscopy Kaiser testing for polyCOOH/functionality quantification, were performed as described.[49]

Peptide conjugation using EDC•HCl activation/coupling chemistry—First, 6.58 nm-sized Yb(III) cation/complex-doped maghemite NPs (2 mL NPs ddH_2O suspension, Fe = 1.543 mg/mL) were placed in a scintillation vial and further diluted to 17 mL using milliQ-purified H_2O. Then, 262 μL (1 eq. relative to the carboxylic acids on the NP surface, as measured by the Kaiser test) of an EDC (1-ethyl-3-(3-dimethylaminopropyl) carbodiimide•HCl, 0.001 mmol) solution in milliQ-purified H_2O (0.725 mg/mL) was added

to the NPs, and the mixture was shaken for 60 min at 15°C in an incubator shaker. Then, the peptide (HSA-28, 1.1 mg, 0.988 μmol, 1 eq. relative to Kaiser test-measured carboxylic acids on the NPs surface, dissolved in 4 mL of milliQ-purified H_2O), was added, and the mixture was shaken overnight at 250 rpm at 15°C.

f-NP purification was achieved by three cycles of sequential centrifugal separation-decantation (3,000 rpm, 10 min, 10°C). The resulting cleaned peptide-conjugated f-NPs were dispersed in 20 mL of H_2O for storage.

The same procedure was performed when using 0.5 eq of EDC (131 μL of 0.725 mg/mL solution, 0.0005 mmol) and the corresponding equivalent quantity of HSA-28 peptide (0.55 mg, 0.0.494μmol, 0.5 equiv.).

Determination of the amount of conjugated HSA-28 to NPs by analytical HPLC —In order to investigate the amount of HSA-28 that was conjugated with nanoparticles, the starting solution of the reactions and all washes were analyzed by analytical HPLC: the concentration of HSA-28 was determined. The calibration curve was used for the determination. The curve was built by measuring the known HSA-28P concentrations (1, 0.1, 0.01, 0.001, and 0.0001 mg/ml). HPLC analysis was performed using a C18 reverse phase column (Phenomenex Luna 5u C18(2); 100 A; 250X4.6 mm) with a Young Lin instrument; YL 9100 HPLC series system attached to a chromatograph manager. A gradient was applied between solvent A (H_2O) and solvent B (CH_3CN). The gradient was A/ B 0 min [100/0], 20 min [0/100], 20–25 min [100/0]. The flow rate was 1 ml/min. λ=220.

MTT cell viability assay

We described this test in our previous publication. [64] Briefly, cells were incubated with MT reagent (2 mg/mL) in growth medium for 30 min at 37°C. The medium was then aspirated, and DMSO was added to solubilize the cells and colored crystals. Absorbance at 570 nm was measured in a SpectraMax M5 spectrophotometer (Sunnyvale, CA, USA). The obtained results were normalized by total protein content in culture cells, which was measured using the Bradford reagent.[65]

Cell counting

Cells were detached by trypsin and colored by Trypan blue. Only uncolored cells were counted. Cell counting proceeded according to Abcam (Cambridge, MA, USA) online protocol for work with a haemocytometer.

Cell lines

INS-1E cells were grown in DMEM (22.5 mM glucose) supplemented with 10% fetal calf serum (FCS), 1 mM glutamine, and antibiotics (100 μg/mL penicillin, 100 μg/mL streptomycin) at 37°C in a 5% CO_2 humidified atmosphere, as described by Pasternak et al. [66] PC-3 and PC-12 were grown and maintained as we previously described.[64]

Cell lysate preparation

Whole cell lysates were prepared as previously described[67] with some minor modifications: the lysis buffer contained 50 mmol/L Tris-HCl, pH 7.5, 1 mmol/L EDTA, 1mmol/L EGTA, 1 mmol/L Na3VO4, 150 mmol/L NaCl, 50 mmol/L NaF, 10 mmol/L sodium-glycerophosphate, 5 mmol/L sodium pyrophosphate, and 1 mmol/L PMSF, supplemented with 0.1% (v/v) IGEPAL, 0.1% (v/v) 2-β-mercaptoethanol, and protease inhibitor cocktail (1:100 dilution). The cells were washed with ice-cold PBS, and 1 ml of lysis buffer was then added at 4°C for 40 min. The resulting cell lysates were centrifuged at 7,800 x g for 30 min at 4°C, and the supernatant fractions were separated and kept at −70°C until used. Protein content in the supernatant was determined by Bradford analysis, using a BSA standard dissolved in the same buffer.

GSIS and Insulin RIA

The assays were performed for INS-1E medium and lysates as previously described.[68]

Induction of oxidative stress

Oxidative stress conditions [69] were induced by supplying glucose oxidase (GO, 50 mU/ml) with high levels of glucose (23.5 mM) to the growing medium of the INS-1E cells. This resulted in an elevated H_2O_2 concentration in the medium (reaching 29.0 ± 9.6 μM in 4 h of incubation). The concentration of H_2O_2 generated by the glucose oxidase/glucose system was determined as described by Thurman et al.[70]

Microscopy

Fluorescent microscopy—INS-1E cells were grown in 6-well plates. HSA-28P labeled by FITC was added to cells for 24 h (control cells were treated only with FITC-labeled nanoparticles). After incubation, cells were gently washed two times with pre-warmed growth medium to remove unbound labeled nanoparticles. After the cells were washed, they were visualized with a CellsSense Live Imaging microscope (Olympus, Tokyo, Japan) operated at 37^0 C.

Confocal microscopy

Cellular localization of HSA-28P: Experiments were conducted in INS-1E cells that were seeded on coverslips in 6-well plates. The cells were incubated with HSA-28P labeled by FITC for 24 h (control cells were treated with naked nanoparticles labeled by FITC). Following incubation, the slides were washed three times with pre-warmed PBS and fixed with formaldehyde (4% in PBS). Subsequently, slides were washed three more times with pre-warmed PBS. The membranes of cells were stained with Alexa Fluor 633 Phalloidin according to the protocol provided by the manufacturer. Slides were washed three times by pre-warmed PBS. Nuclei were stained with DAPI according to the protocol supplied by the manufacturer. Fluorescent signals were visualized with a Confocal- Zeiss microscope equipped with a 60x/1.4 objective (Oberkochen, Germany).

The effect of HSA-28P on the C-peptide level: Cells were grown as described above. Slides were incubated with HSA-28P or with non-coated nanoparticles for 24 h. The level of

C-peptide was determined by immunocytochemistry using anti-C-peptide antibody. Thereafter, slides were fixed with formaldehyde as described above. Cell membranes and nuclei were stained as previously described. Visualization of fluorescent signals proceeded as described above.

The effect of HSA-28P on the glucagon level: Cells were grown as described above. Slides were incubated with HSA-28P or with non-coated nanoparticles for 24 h. The level of glucagon was determined by immunocytochemistry using anti-glucagon antibody. Thereafter, slides were fixed with formaldehyde as described above. Cell membranes and nuclei were stained as previously described. Visualization of fluorescent signals proceeded as described above. Glucagon that was conjugated to the polylysine layer was used as a positive control. Slides were covered by polylysine according to the instructions of the product's manufacturer.

Flow cytometry: INS-1E cells were seeded in 12-well plates. The cells were incubated with HSA-28P, "naked" nanoparticles or HSA-28 for 24 h. After the incubation the cells were exposed to fluorescent labeled antibody against an extracellular epitope of neurexin 1α according to the manufacturer`s protocol. The fluorescent signal was quantified using Gallios Fluorescence Activated Cell Sorter (Beckman Coulter Life Sciences, USA).

Mice

C57 black mice were purchased from Jackson Laboratories (Bar Harbor, ME, USA). The animals were housed under standard conditions: constant temperature (22±1°C), humidity (relative, 40%), and a 12 h light/dark cycle and were allowed free access to food and water. Bar-Ilan University is an Association for Assessment and Accreditation of Laboratory Animal Care (AAALAC) internationally accredited institution.

Isolation of mouse islets

Mice (6 in total) were euthanized by cervical dislocation; the mouse torso was saturated with 70% ethanol. The abdominal cavity was opened completely from anus to diaphragm. The body and tail of the pancreas were removed and separated from fat and large vessels. The pancreas was washed once with HBSS solution and cut into small pieces of approximately 2×3 mm with a scissors. After an additional wash with HBSS solution, the pieces of pancreas were placed in two 50 ml Falcon tubes containing 4 ml of a freshly prepared solution of collagenase (2 mg/ml). After vigorous shaking at 37°C for approximately 20 min, the collagenase digestion was interrupted by adding 45 ml of ice-chilled HBSS solution. The digested pancreatic tissue was spinned down at 330x g for 3 minutes. Supernatant was removed again and an additional 45 mL of "islet media" was added and spinned down at 330x g for 3 minutes. The histopaque was decanted and the tubes were inverted to drain on an absorbent paper towel for 1 min. The pellet was resuspended in 20 ml for each tube in cold 30% Ficoll solution. The histopaque was overlaid with 10 ml of HBSS and centrifuged at 900 x g for 12 min. The islets floated at the interface of the Ficoll and media. Islets were collected from the interface, and transferred to a fresh 50 ml tube. Islets were washed twice with HBSS solution and spinned down at 330x g for 3 minutes. The resulting pellet was suspended in 10 ml "islet medium" and passed through an inverted 100

μm filter and then through an inverted 30 μm filter. Islets were rinsed into a Petri dish by pipetting 10 ml of the RPMI 1640 medium supplied with 10% heat-inactivated FBS, 1% Pen-Strep solution, and 11 mM glucose through the filter while holding it right side up over the dish. Around 300 islets per dish were seeded. Islets were then cultured at 37°C with 5% CO_2 for 2 days.

Glucose-Stimulated Insulin Secretion (GSIS) test in islets

After incubation with test compounds in RPMI 1640 medium, the islets were taken to GSIS. The medium was changed to KRBB supplemented with 2.5 mM glucose (minimal volume). Islets were preincubated in KRBB for an additional hour and then the medium was changed to either 2.5 mM or 16.7 mM glucose KRBB medium. Islets were incubated for 1 hour in different glucose concentrations. 10 mM of L-Arginine was used as a positive control. At the end of incubation, the medium was collected and spinned down at 500x g for 5 minutes. The supernatent was used for determining the insulin level in the medium. Islets were washed by cold KRBB and lysated by adding lysis buffer (RIPA buffer supplemented with protease inhibitors) and shaken for 30 minutes in a cold room. Using “policemen”, the lysate was collected and spinned at 10.000 x g for 10 minutes. The resulting supernatant was used to determine the insulin contents and the total protein level.

Determination of the insulin level in mouse islets

Frozen islets medium or lysates were thawed on ice and diluted with water (a typical dilution for the lysate was 300x and for the supernatant – 5x). Mouse Ultrasensitive Insulin ELISA kit, ALPCO (Salem, New Hampshire, USA) was used for insulin level determination as described in the manufacturer’s protocol. The signal was determined by a SpectraMax M5 spectrophotometer. The concentrations of insulin in the samples were normalized by the total protein determined by Pierce BCA Protein Assay Kit according to manufacturer instructions.

Statistical analysis

Statistical significance *, # ($p < 0.05$) was calculated among the various experimental groups using Student’s t-test (two tailed). Results are given as the mean ± SEM (n =3–6). The QuickCalcs online service (GraphPad Software: http://www.graphpad.com/quickcalcs/ttest1.cfm) was used for statistical evaluations.

Supplementary Material

Refer to Web version on PubMed Central for supplementary material.

Acknowledgments

Funding Sources

This study was supported by a Bar-Ilan University new faculty grant (20094), a D-cure (Diabetes Care in Israel) Young Investigator Award (182013), and a NOFAR program (53103, Israel Ministry of Industry) for A.G. The Israel Science Foundation (117/2014) provided a grant for A.G and J-P.L. In addition, S. K. is thankful for the support of her work by the Wolf Foundation (SK1010). S.D.C. was supported by NIH/NIDDK grant R01DK080971. This work was also funded by the VIIth Framework RTD European Project (FP7– 530 NMP-2010-LARGE-4 area) – Large Collaborative Projects – Project 531 SaveMe (no. 263307) for J-P.L.

ABBREVIATIONS

AAS	atomic absorption spectroscopy
BCA	bicinchoninic acid
BOP	Benzotriazol-1-yloxy)tris(dimethylamino)phosphonium hexafluorophosphate
CAN	Ceric Ammonium Nitrate
DIEA	diethyl isopropyl amine
DMEM	Dulbecco's Modified Eagle Medium
DMF	dimethylformamide
DMSO	dimethyl sulfoxide
DLS	dynamic light scattering
EDC	N-(3-dimethylaminopropyl)-*N*′-ethylcarbodiimide hydrochloride
GO	glucose oxidase
GSIS	glucose-stimulated insulin secretion
FCS	fetal calf serum
FITC	fluorescein isothiocyanate; Hank's Balanced Salt Solution Krebs-Ringer bicarbonate buffer
ICP-AES	inductively coupled plasma atomic emission spectroscopy
MD	molecular dynamics
MTT	3-(4,5-Dimethylthiazol-2-yl)-2,5-Diphenyltetrazolium Bromide
NVT	constant number (N), volume (V), temperature (T)
NPT	constant number (N), pressure (P), temperature (T)
NP	nanoparticles
NL	neuroligins
NX	neurexins
PBS	phosphate buffered saline
PEG	polyethylene glycol
RIPA	radioimmunoprecipitation assay buffer

TBTU	N,N,N′,N′-tetramethyl-O-(benzotriazol-1-yl)uronium tetrafluoroborate
TCA	trichloric acetic acid
TEM-EDAXS	transmission electron microscopy-energy-dispersive X-spectroscopy
THF	tetrahydrofuran
T1DM and T2DM	type one and type two diabetes
VdW	van der Waals
XPS	X-ray photoelectron spectroscopy

References

(1). Araujo TG, Oliveira AG, Saad MJ. Insulin-Resistance-Associated Compensatory Mechanisms of Pancreatic Beta Cells: a Current Opinion Front. Endocrinol. (Lausanne, Switzerland). 2013; 4:146.

(2). Vetere A, Choudhary A, Burns SM, Wagner BK. Targeting the Pancreatic Beta-Cell to Treat Diabetes Nat. Rev. Drug Discovery. 2014; 13:278–289. [PubMed: 24525781]

(3). Ludvigsson J. The Latest Pharmacotherapy Options for Type 1 Diabetes Expert Opin. Pharmacother. 2014; 15:37–49. [PubMed: 24289822]

(4). Halban PA, Polonsky KS, Bowden DW, Hawkins MA, Ling C, Mather KJ, Powers AC, Rhodes CJ, Sussel L, Weir GC. Beta-Cell Failure in Type 2 Diabetes: Postulated Mechanisms and Prospects for Prevention and Treatment Diabetes Care. 2014; 37:1751–1758. [PubMed: 24812433]

(5). Mudaliar S. Choice of Early Treatment Regimen and Impact on Beta-Cell Preservation in Type 2 Diabetes *Int. J. Clin*. Pract.. 2013; 67:876–887. [PubMed: 23952467]

(6). Weir GC, Aguayo-Mazzucato C, Bonner-Weir S. Beta-Cell Dedifferentiation in Diabetes Is Important, but What Is It? Islets. 2013; 5:233–237. [PubMed: 24356710]

(7). Lundh M, Scully SS, Mandrup-Poulsen T, Wagner BK. Small-Molecule Inhibition of Inflammatory Beta-Cell Death *Dia*betes, Obes. Metab.. 2013; 15:176–184. [PubMed: 24003935]

(8). Shen J, Cheng Y, Han Q, Mu Y, Han W. Generating Insulin-Producing Cells for Diabetic Therapy: Existing Strategies and New Development Ageing Res. Rev. 2013; 12:469–478. [PubMed: 23318683]

(9). Woodford C, Zandstra PW. Tissue Engineering 2.0: Guiding Self-Organization During Puripotent Stem Cell Differentiation *Curr. Opin*. Biotechnol.. 2012; 23:810–819. [PubMed: 22444525]

(10). Orlando G, Gianello P, Salvatori M, Stratta RJ, Soker S, Ricordi C, Dominguez-Bendala J. Cell Replacement Strategies Aimed at Reconstitution of the Beta-Cell Compartment inType 1 Diabetes Diabetes. 2014; 63:1433–1444. [PubMed: 24757193]

(11). Schiesser JV, Wells JM. Generation of Beta Cells from Human Pluripotent Stem Cells: Are We There Yet? Ann. N. Y. Acad. Sci. 2014; 1311:124–137. [PubMed: 24611778]

(12). Kelly OG, Chan MY, Martinson LA, Kadoya K, Ostertag TM, Ross KG, Richardson M, Carpenter MK, D'Amour KA, Kroon E, Moorman M, Baetge EE, Bang AG. Cell-Surface Markers for the Isolation of Pancreatic Cell Types Derived from Human Embryonic Stem Cells Nat. Biotechnol. 2011; 29:750–756. [PubMed: 21804561]

(13). Calafiore R, Montanucci P, Basta G. Stem Cells for Pancreatic Beta-Cell Replacement in Diabetes Mellitus: Actual Perspectives . *Curr. Opin. Organ Transplant.*. 2014; 19:162–168. [PubMed: 24553500]

(14). Lin CC, Anseth KS. Cell-Cell Communication Mimicry with Poly(ethylene glycol) Hydrogels for Enhancing Beta-Cell Function Proc. Natl. Acad. Sci. U. S. A. 2011; 108:6380–6385. [PubMed: 21464290]

(15). Salvay DM, Rives CB, Zhang X, Chen F, Kaufman DB, Lowe WL Jr., Shea LD. Extracellular Matrix Protein-Coated Scaffolds Promote the Reversal of Diabetes after Extrahepatic Islet Transplantation Transplantation. 2008; 85:1456–1464. [PubMed: 18497687]

(16). Park GE, Pattison MA, Park K, Webster TJ. Accelerated Chondrocyte Functions on NaOH-Treated PLGA Scaffolds Biomaterials. 2005; 26:3075–3082. [PubMed: 15603802]

(17). Daoud JT, Petropavlovskaia MS, Patapas JM, Degrandpre CE, Diraddo RW, Rosenberg L, Tabrizian M. Long-Term in Vitro Human Pancreatic Islet Culture Using Three-Dimensional Microfabricated Scaffolds Biomaterials. 2011; 32:1536–1542. [PubMed: 21093908]

(18). Wang X, Ye K. Three-Dimensional Differentiation of Embryonic Stem Cells into Islet-Like Insulin-Producing Clusters Tissue Eng. 2009; 15:1941–1952.

(19). Bosco D, Orci L, Meda P. Homologous but not Heterologous Contact Increases the Insulin Secretion of Individual Pancreatic B-Cells Exp. Cell Res. 1989; 184:72–80. [PubMed: 2676573]

(20). Hallengren B, Falorni A, Landin-Olsson M, Lernmark A, Papadopoulos KI, Sundkvist G. Islet Cell and Glutamic Acid Decarboxylase Antibodies in Hyperthyroid Patients: at Diagnosis and Following Treatment J. Intern. Med. 1996; 239:63–68. [PubMed: 8551202]

(21). Liu X, Yan F, Yao H, Chang M, Qin J, Li Y, Wang Y, Pei X. Involvement of RhoA/ROCK in Insulin Secretion of Pancreatic Beta-Cells in 3D Culture Cell Tissue Res. 2014; 358:359–369. [PubMed: 25129107]

(22). Bhandari DR, Seo KW, Sun B, Seo MS, Kim HS, Seo YJ, Marcin J, Forraz N, Roy HL, Larry D, Colin M, Kang KS. The Simplest Method for in Vitro Beta-Cell Production from Human Adult Stem Cells Differentiation. 2011; 82:144–152. [PubMed: 21782317]

(23). Guo-Parke H, McCluskey JT, Kelly C, Hamid M, McClenaghan NH, Flatt PR. Configuration of Electrofusion-Derived Human Insulin-Secreting Cell Line as Pseudoislets Enhances Functionality and Therapeutic Utility Endocrinology. 2012; 214:257–265.

(24). Jain R, Lammert E. Cell-Cell Interactions in the Endocrine Pancreas Diabetes. Obes. Metab. 2009; 11:159–167.

(25). Esni F, Taljedal IB, Perl AK, Cremer H, Christofori G, Semb H. Neural Cell Adhesion Molecule (N-CAM) Is Required for Cell Type Segregation and Normal Ultrastructure in Pancreatic Islets Cell Biol. 1999; 144:325–337.

(26). Easom RA. Beta-Granule Transport and Exocytosis Semin. Cell Dev. Biol. 2000; 11:253–266. [PubMed: 10966859]

(27). Craig AM, Kang Y. Neurexin-Neuroligin Signaling in Synapse Development *Curr. Opin. Neurobiol.*. 2007; 17:43–52. [PubMed: 17275284]

(28). Bang ML, Owczarek S. A Matter of Balance: Role of Neurexin and Neuroligin at the Synapse Neurochem. Res. 2013; 38:1174–1189. [PubMed: 23559421]

(29). Koehnke J, Jin X, Trbovic N, Katsamba PS, Brasch J, Ahlsen G, Scheiffele P, Honig B, Palmer AG 3rd, Shapiro L. Crystal Structures of Beta-Neurexin 1 and Beta-Neurexin 2 Ectodomains and Dynamics of Splice Insertion Sequence 4 Structure. 2008; 16:410–421. [PubMed: 18334216]

(30). Reissner C, Runkel F, Missler M. Neurexins Genome Biol. 2013; 14:213. [PubMed: 24083347]

(31). Varoqueaux F, Aramuni G, Rawson RL, Mohrmann R, Missler M, Gottmann K, Zhang W, Sudhof TC, Brose N. Neuroligins Determine Synapse Maturation and Function Neuron. 2006; 51:741–754. [PubMed: 16982420]

(32). Cline H. Synaptogenesis: a Balancing Act between Excitation and Inhibition Curr. Biol. 2005; 15:R203–R205. [PubMed: 15797012]

(33). Rothwell PE, Fuccillo MV, Maxeiner S, Hayton SJ, Gokce O, Lim BK, Fowler SC, Malenka RC, Sudhof TC. Autism-Associated Neuroligin-3 Mutations Commonly Impair Striatal Circuits to Boost Repetitive Behaviors Cell. 2014; 158:198–212. [PubMed: 24995986]

(34). Chanda S, Marro S, Wernig M, Sudhof TC. Neurons Generated by Direct Conversion of Fibroblasts Reproduce Synaptic Phenotype Caused by Autism-Associated Neuroligin-3 Mutation Proc. Natl. Acad. Sci. U. S. A. 2013; 110:16622–16627. [PubMed: 24046374]

(35). Mackowiak M, Mordalska P, Wedzony K. Neuroligins, Synapse Balance and Neuropsychiatric Disorders Pharmacol. Rep. 2014; 66:830–835. [PubMed: 25149987]

(36). Treutlein B, Gokce O, Quake SR, Sudhof TC. Cartography of Neurexin Alternative Splicing Mapped by Single-Molecule Long-Read mRNA Sequencing Proc. Natl. Acad. Sci. U. S. A. 2014; 111:E1291–E1299. [PubMed: 24639501]

(37). Graf ER, Zhang X, Jin SX, Linhoff MW, Craig AM. Neurexins Induce Differentiation of GABA and Glutamate Postsynaptic Specializations via Neuroligins Cell. 2004; 119:1013–1026. [PubMed: 15620359]

(38). Dean C, Scholl FG, Choih J, DeMaria S, Berger J, Isacoff E, Scheiffele P. Neurexin Mediates the Assembly of Presynaptic Terminals Nat. Neurosci. 2003; 6:708–716. [PubMed: 12796785]

(39). Chowdhury A, Satagopam VP, Manukyan L, Artemenko KA, Fung YM, Schneider R, Bergquist J, Bergsten P. Signaling in Insulin-Secreting MIN6 Pseudoislets and Monolayer Cells J. Proteome Res. 2013; 12:5954–5962. [PubMed: 24006944]

(40). Chowdhury A, Dyachok O, Tengholm A, Sandler S, Bergsten P. Functional Differences between Aggregated and Dispersed Insulin-Producing Cells Diabetologia. 2013; 56:1557–1568. [PubMed: 23604550]

(41). Mosedale M, Egodage S, Calma RC, Chi NW, Chessler SD. Neurexin-1alpha Contributes to Insulin-Containing Secretory Granule Docking J. Biol. Chem. 2012; 287:6350–6361. [PubMed: 22235116]

(42). Suckow AT, Zhang C, Egodage S, Comoletti D, Taylor P, Miller MT, Sweet IR, Chessler SD. Transcellular Neuroligin-2 Interactions Enhance Insulin Secretion and Are Integral to Pancreatic Beta Cell Function J. Biol. Chem. 2012; 287:19816–19826. [PubMed: 22528485]

(43). Suckow AT, Comoletti D, Waldrop MA, Mosedale M, Egodage S, Taylor P, Chessler SD. Expression of Neurexin, Neuroligin, and Their Cytoplasmic Binding Partners in the Pancreatic Beta-Cells and the Involvement of Neuroligin in Insulin Secretion Endocrinology. 2008; 149:6006–6017. [PubMed: 18755801]

(44). Zhang C, Suckow AT, Chessler SD. Altered Pancreatic Islet Function and Morphology in Mice Lacking the Beta-Cell Surface Protein Neuroligin-2 PLoS One. 2013; 8:e65711. [PubMed: 23776533]

(45). Israel LL, Lellouche E, Kenett RS, Green O, Michaeli S, Lellouche J-P. Ce 3/4+ Cation-Functionalized Maghemite Nanoparticles towards siRNA-Mediated Gene Silencing J. Mater. Chem. B. 2014; 2:6215–6225.

(46). Gjorlund MD, Nielsen J, Pankratova S, Li S, Korshunova I, Bock E, Berezin V. Neuroligin-1 Induces Neurite Outgrowth through Interaction with Neurexin-1beta and Activation of Fibroblast Growth Factor Receptor-1 FASEB J. 2012; 26:4174–4186. [PubMed: 22750515]

(47). van der Kooij MA, Fantin M, Kraev I, Korshunova I, Grosse J, Zanoletti O, Guirado R, Garcia-Mompo C, Nacher J, Stewart MG, Berezin V, Sandi C. Impaired Hippocampal Neuroligin-2 Function by Chronic Stress or Synthetic Peptide Treatment is Linked to Social Deficits and Increased Aggression Neuropsychopharmacology. 2014; 39:1148–1158. [PubMed: 24213355]

(48). Israel LL, Karimi F, Bianchessi S, Scanziani E, Passoni L, Matteoli M, Langström B, Lellouche J-P. Surface Metal Cation Doping of Maghemite Nanoparticles: Modulation of MRI Relaxivity Features and Chelator-Free 68Ga-Radiolabelling for Dual MRI-PET Imaging Mater. Res. Express. 2015; 2:095009.

(49). Israel LL, Kovalenko EI, Boyko AA, Sapozhnikov AM, Rosenberger I, Kreuter J, Passoni L, Lellouche JP. Towards Hybrid Biocompatible Magnetic rHuman Serum Albumin-Based Nanoparticles: Use of Ultra-Small (CeLn)3/4+ Cation-Doped Maghemite Nanoparticles as Functional Shell Nanotechnology. 2015; 26:045601. [PubMed: 25556693]

(50). Massart R, Dubois E, Cabuil V, Hasmonay E. Preparation and Properties of Monodisperse magnetic Fluids J. Magn. Magn. Mater. 1995; 149:1–5.

(51). Sarin VK, Kent SB, Tam JP, Merrifield RB. Quantitative Monitoring of Solid-Phase Peptide Synthesis by the Ninhydrin Reaction Anal. Biochem. 1981; 117:147–157. [PubMed: 7316187]

(52). Grifman M, Galyam N, Seidman S, Soreq H. Functional Redundancy of Acetylcholinesterase and Neuroligin in Mammalian Neuritogenesis Proc. Natl. Acad. Sci. U. S. A. 1998; 95:13935–13940. [PubMed: 9811904]

(53). Vincent M, Guz Y, Rozenberg M, Webb G, Furuta M, Steiner D, Teitelman G. Abrogation of Protein Convertase 2 Activity Results in Delayed Islet Cell Differentiation and Maturation, Increased Alpha-Cell Proliferation, and Islet Neogenesis Endocrinology. 2003; 144:4061–4069. [PubMed: 12933680]

(54). Schisler JC, Jensen PB, Taylor DG, Becker TC, Knop FK, Takekawa S, German M, Weir GC, Lu D, Mirmira RG, Newgard CB. The Nkx6.1 Homeodomain Transcription Factor Suppresses Glucagon Expression and Regulates Glucose-Stimulated Insulin Secretion in Islet Beta Cells Proc. Natl. Acad. Sci. U. S. A. 2005; 102:7297–7302. [PubMed: 15883383]

(55). Bollheimer LC, Wrede CE, Rockmann F, Ottinger I, Scholmerich J, Buettner R. Glucagon Production of the Rat Insulinoma Cell Line INS-1-A Quantitative Comparison with Primary Rat Pancreatic Islets Biochem. Biophys. Res. Commun. 2005; 330:327–332. [PubMed: 15781268]

(56). Poitout V, Olson LK, Robertson RP. Insulin-Secreting Cell Lines: Classification, Characteristics and Potential Applications Diabetes Metab. 1996; 22:7–14. [PubMed: 8697299]

(57). Lacy PE, Kostianovsky M. Method for the Isolation of Intact Islets of Langerhans from the Rat Pancreas Diabetes. 1967; 16:35–39. [PubMed: 5333500]

(58). Accelrys Software Inc., D. S. M. E., Release 4.0, San Diego: Accelrys Software Inc. **2013**.

(59). Hess B, Kutzner C, van der Spoel D, Lindahl E. GROMACS 4: Algorithms for Highly Efficient, Load-Balanced, and Scalable Molecular Simulation J. Chem. Theory Comput. 2008; 4:435–447. [PubMed: 26620784]

(60). Lindorff-Larsen K, Piana S, Palmo K, Maragakis P, Klepeis JL, Dror RO, Shaw DE. Improved Side-ChainTorsion Potentials for the Amber ff99SB Protein Force Field Proteins. 2010; 78:1950–1958. [PubMed: 20408171]

(61). Hockney RW, Goel SP, Eastwood JW. Quiet High-Resolution Computer Models of a Plasma J. Comput. Phys. 1974; 14:148–158.

(62). Essmann U, Perera L, Berkowitz ML, Darden T, Lee H, Pedersen LG. A Smooth Particle Mesh Ewald Method J. Chem. Phys. 1995; 103:8577–8593.

(63). Hess B, Bekker H, Berendsen HJC, Fraaije JGEM. LINCS: A Linear Constraint Solver for Molecular Simulations J. Comput. Chem. 1997; 18:1463–1472.

(64). Munder A, Moskovitz Y, Redko B, Levy AR, Ruthstein S, Gellerman G, Gruzman A. Antiproliferative Effect of Novel Aminoacridine-based Compounds Med. Chem. 2015; 11:373–382. [PubMed: 25524547]

(65). Bradford MM. A Rapid and Sensitive Method for the Quantitation of Microgram Quantities of Protein Utilizing the Principle of Protein-Dye Binding Anal. Biochem. 1976; 72:248–254. [PubMed: 942051]

(66). Pasternak L, Meltzer-Mats E, Babai-Shani G, Cohen G, Viskind O, Eckel J, Cerasi E, Sasson S, Gruzman A. Benzothiazole Derivatives Augment Glucose Uptake in Skeletal Muscle Cells and Stimulate Insulin Secretion From Pancreatic Beta-Cells via AMPK Activation Chem. Commun. (Cambridge, U. K.). 2014; 50:11222–11225.

(67). Daniel B, Green O, Viskind O, Gruzman A. Riluzole Increases the Rate of Glucose Transport in L6 Myotubes and NSC-34 Motor Neuron-Like Cells via AMPK Pathway Activation Amyotrophic Lateral Scler. Frontotemporal Degener. 2013; 14:434–443.

(68). Cohen G, Shamni O, Avrahami Y, Cohen O, Broner EC, Filippov-Levy N, Chatgilialoglu C, Ferreri C, Kaiser N, Sasson S. Beta Cell Response to Nutrient Overload Involves Phospholipid Remodelling and Lipid Peroxidation Diabetologia. 2015; 58:1333–1343. [PubMed: 25810039]

(69). Shapira R, Rudnick S, Daniel B, Viskind O, Aisha V, Richman M, Ayasolla KR, Perelman A, Chill JH, Gruzman A, Rahimipour S. Multifunctional Cyclic D,L-Alpha-Peptide Architectures Stimulate non-Insulin Dependent Gucose Uptake in Skeletal Muscle Cells and Protect Them against Oxidative Stress J. Med. Chem. 2013; 56:6709–6718. [PubMed: 23984871]

(70). Thurman RG, Scholz R. The Role of Hydrogen Peroxide and Catalase in Hepatic Microsomal Ethanol Oxidation Drug Metab. Dispos. 1973; 1:441–448. [PubMed: 4149416]

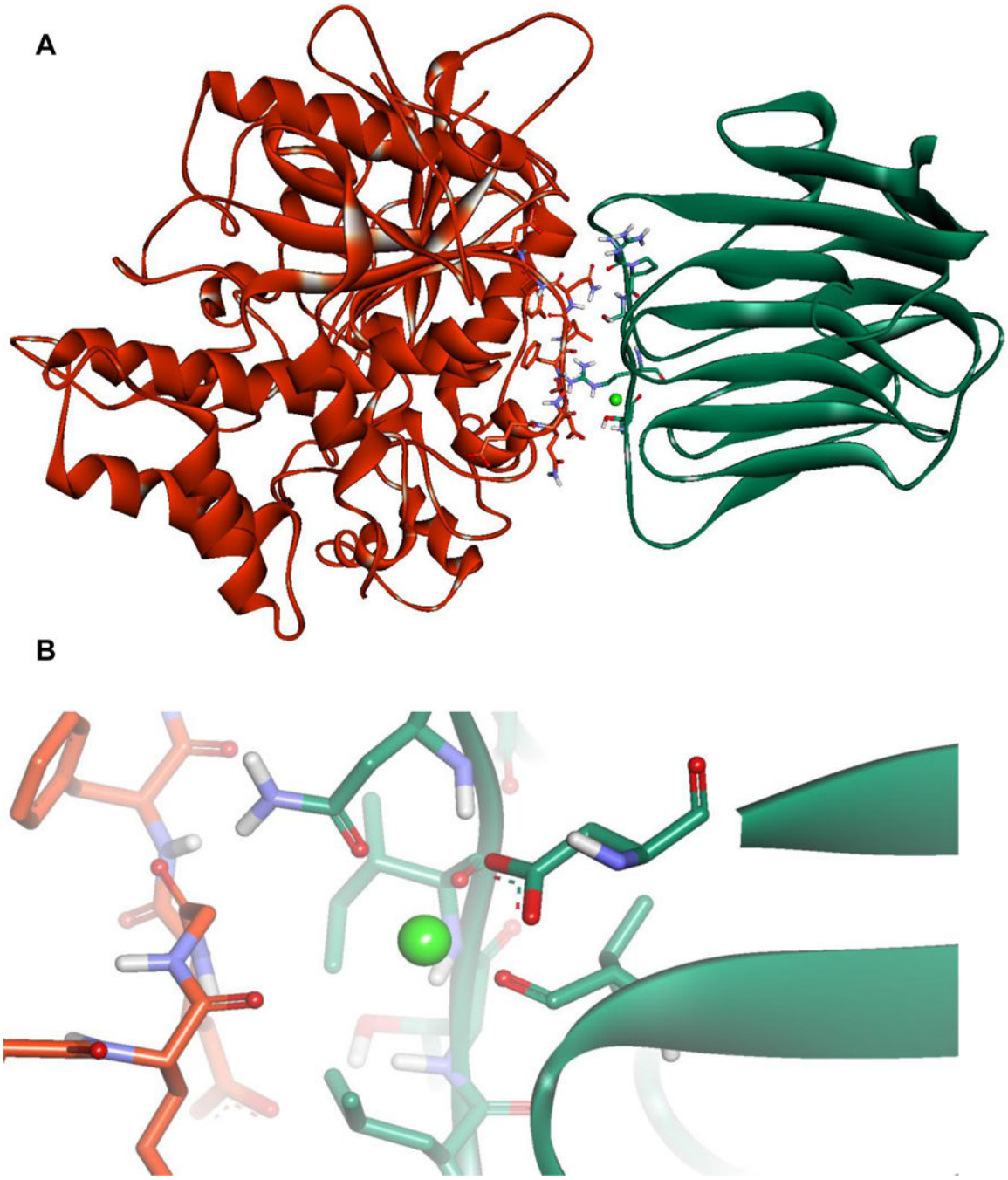

Figure 1. Structure of the NX-1 / NL-4 complex

A. *The NX-1 / NL-4 complex (PDB code 2WQZ).* The residues responsible for the hydrogen bonds between NX-1 and NL-4 are shown in stick representation (Thr 235, Pro 106, Ser 107, Arg 109 of NX-1, and residues Glu 361 and Asn 364 of NL-4. **B**. Coordination of calcium ion by residues Asp 137, Asn 238, Val 154, and Ile 236 of NX-1 and residues Gln 359 and Gly 360 of NL-4.

A

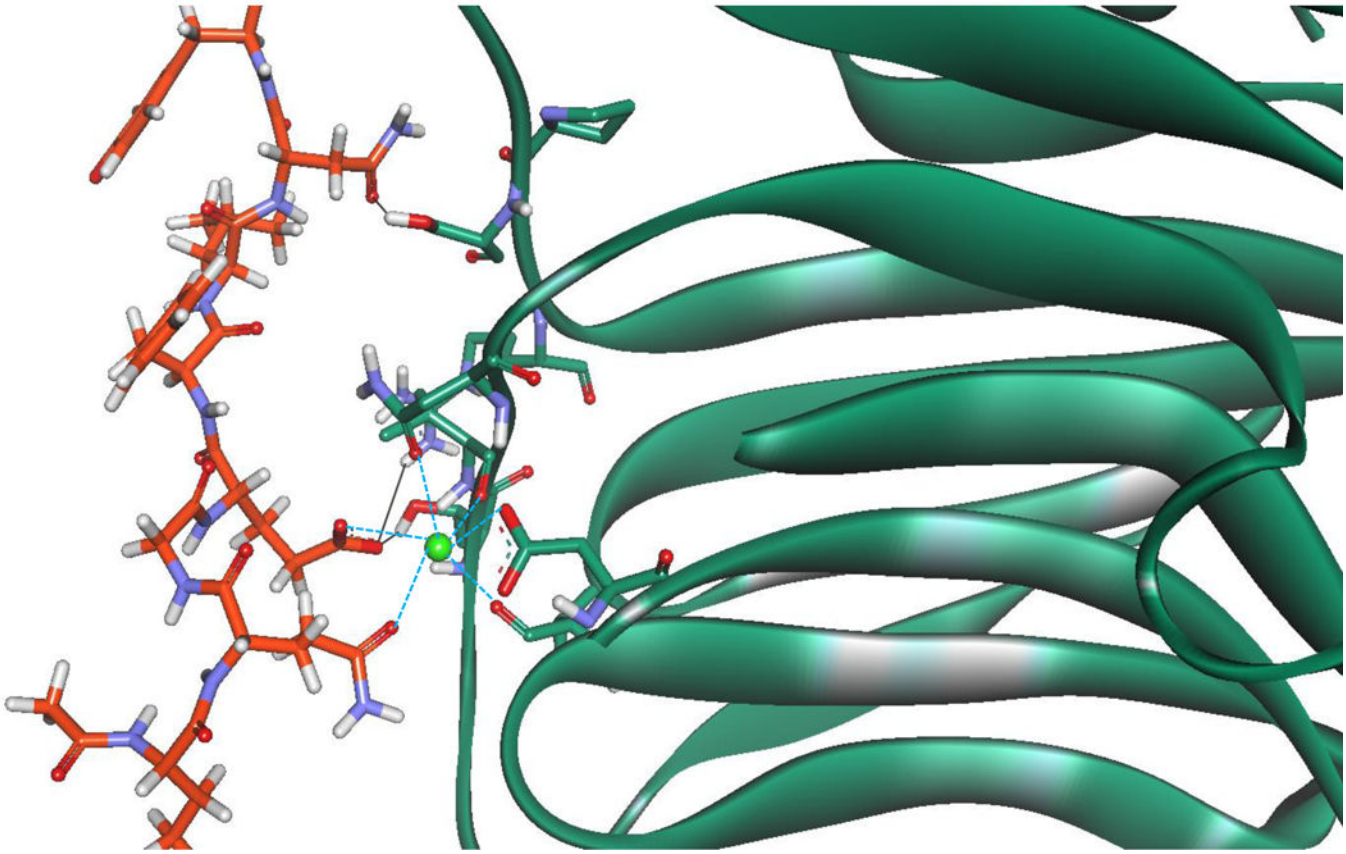

B

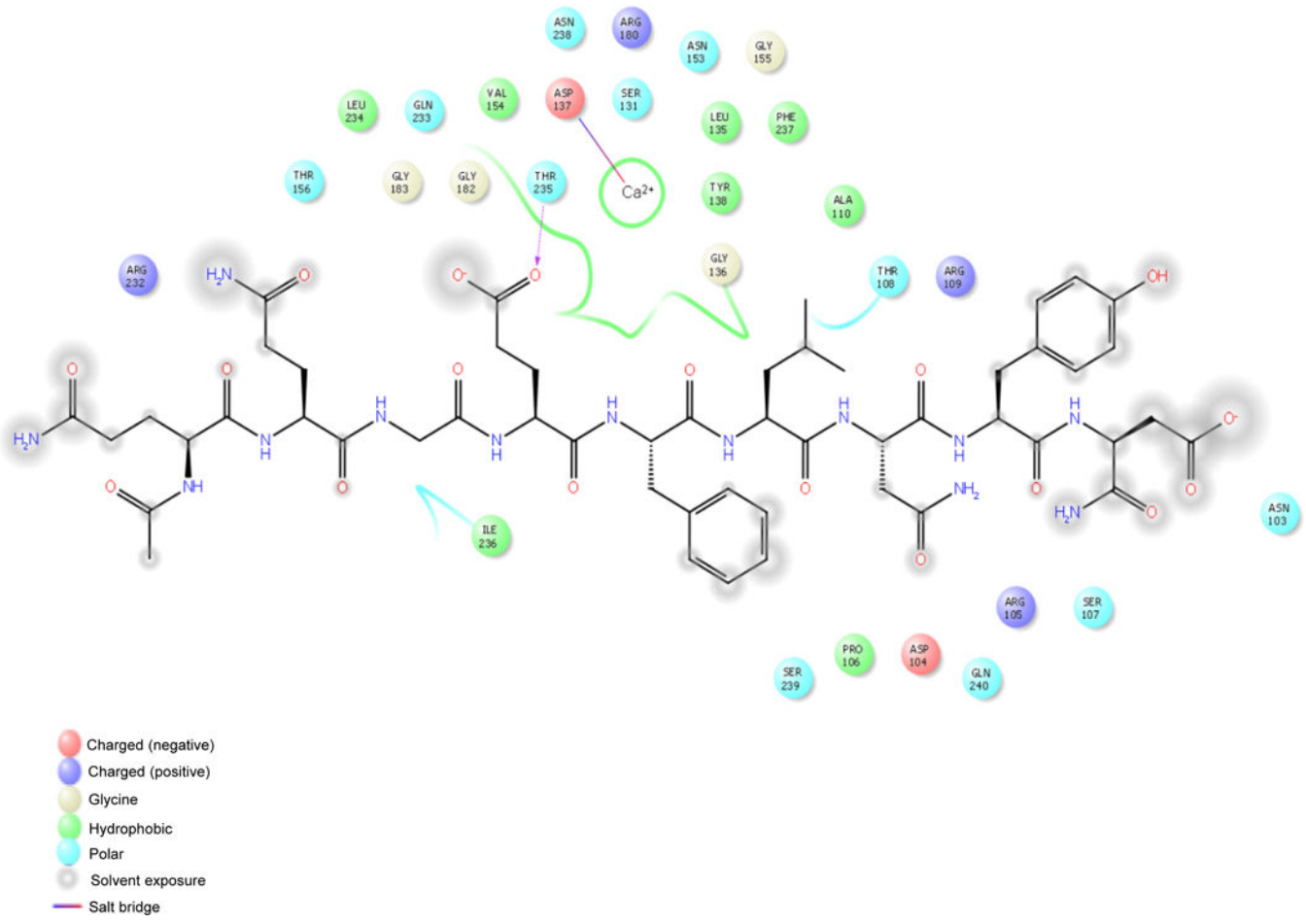

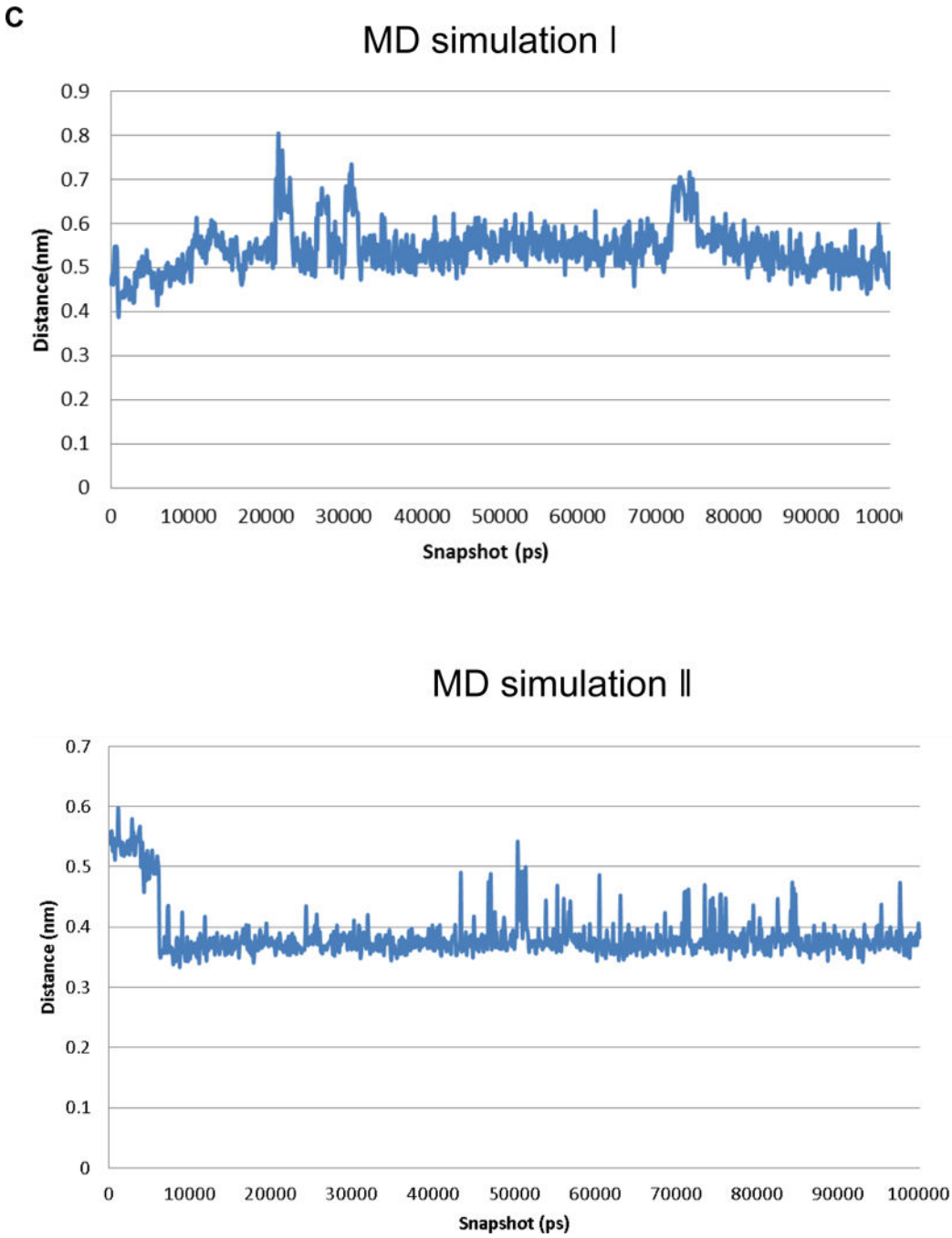

Figure 2. Molecular Dynamics (MD)-based analysis of the HSA-28 / NX-1 interactions

A. Role of the calcium ion and of hydrogen bonds in maintaining the interaction between HSA-28 and NX-1. Snapshot from the MD shows the interactions between the peptide, the calcium, and NX-1 are depicted in blue. Hydrogen bonds are shown in black. **B**. 2D diagram showing the interaction between HSA-28 and NX-1. **C**. Distance between HSA-28 (Gln 359 and Gly 360) and the calcium ion as a function of simulation times in both 2 MD simulations. The distance has converged after ~5000 ps, demonstrating a stable interaction between the two partners.

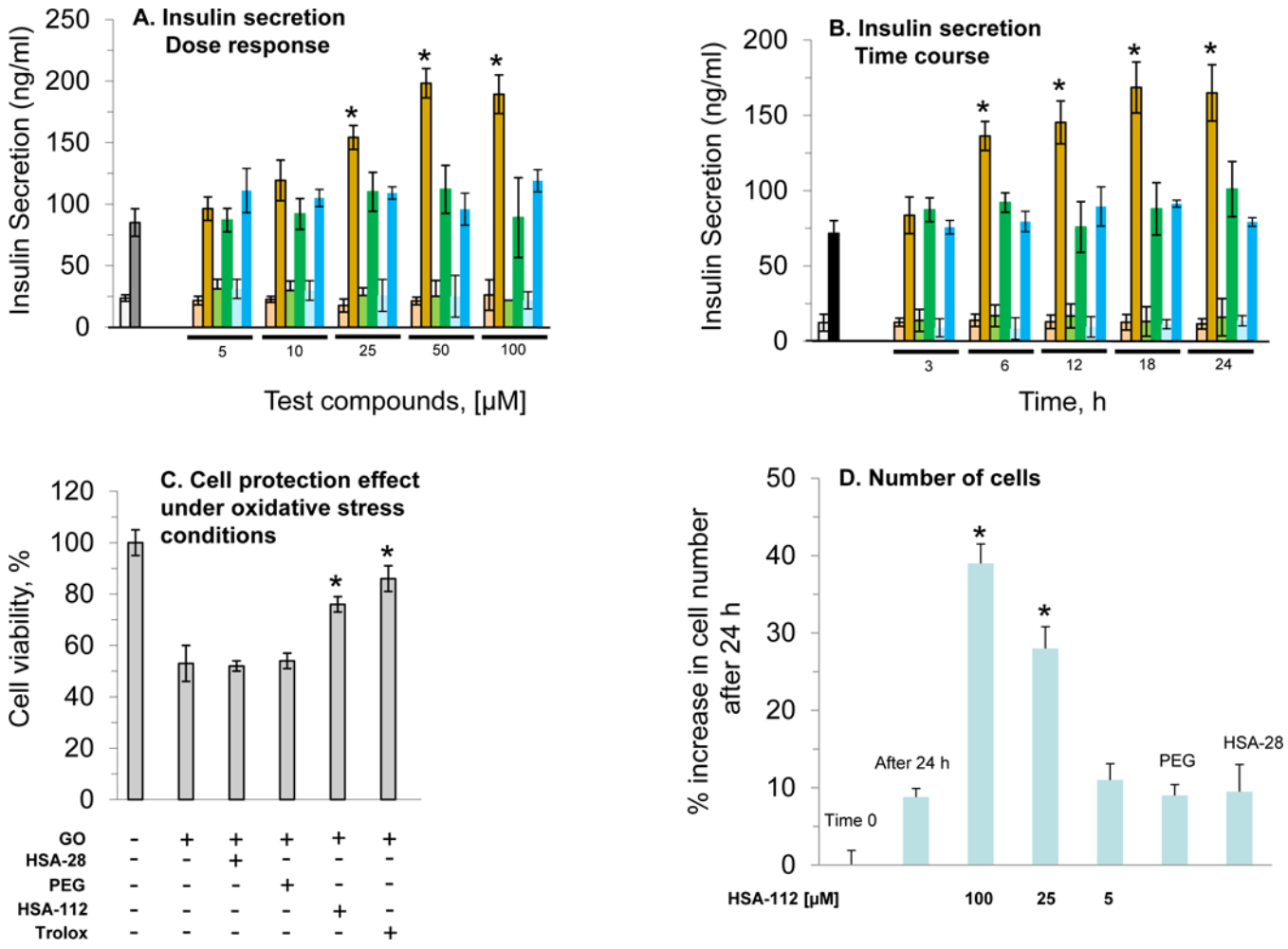

Figure 3. Evaluation of the biological activity of HSA-112 in INS-1E cells

A Dose–response analysis of the effect of HSA-112 on the rate of insulin secretion in INS-1E cells. The INS-1E cells were grown and treated with increasing doses of HSA-112 for 24 h, as described in Methods. Subsequently, cells were mixed with different concentrations of HSA-112, as indicated in the graph (red columns), PEG_{2000} (green columns), and free peptide (blue columns) and were seeded in 12-well plates. After 24 h glucose stimulated insulin secretion (GSIS) was tested in the presence of 2.5 mM (weak color bars) or 16.7 mM (strong color bars) glucose. **B**. Time-course analysis of the effect of HSA-112 on the rate of insulin secretion in INS-1E cells. The INS-1E cells were prepared for the experiment as described above with 50 μM of HSA-112, PEG_{2000}, or free peptide. After incubation, as indicated in the graph, analysis of GSIS was performed as described above. **C**. The cell protective effect of HSA-112 under oxidative stress conditions. Cells were prepared for the experiment as described in Methods. Trolox was used as a positive control at a concentration of 100 μM. The oxidative stress was induced in the tissue culture, as described in Methods. Standard MTT analysis (also described in Methods) was used for evaluating the effect of HSA-112 on cell viability. **D**. *INS-1E cell proliferation.* Cells were prepared for the experiment as described above. After 24 h the cells were colored by trypan blue and counted as described in Methods *$p<0.05$, n=6. MEAN±SE.

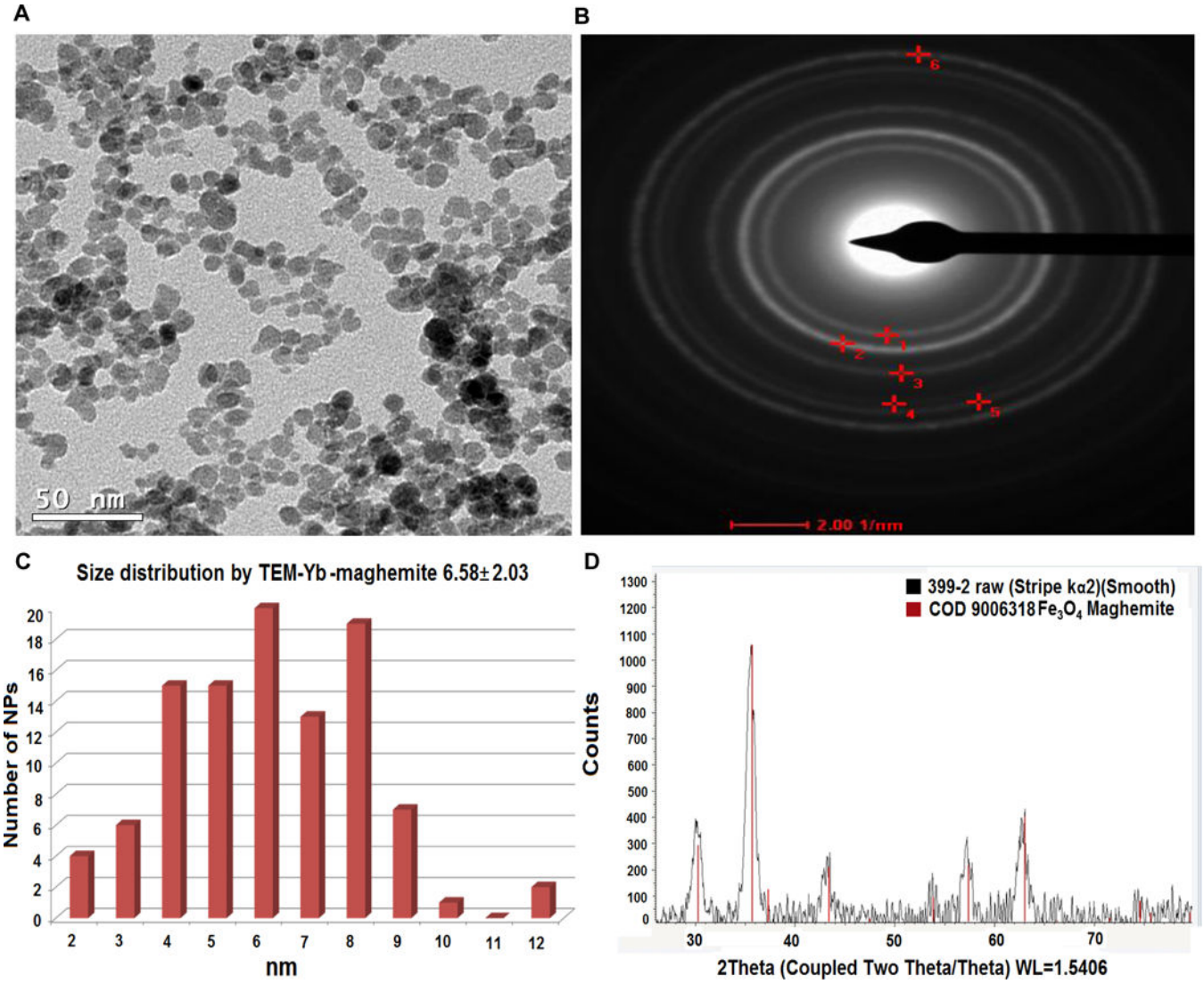

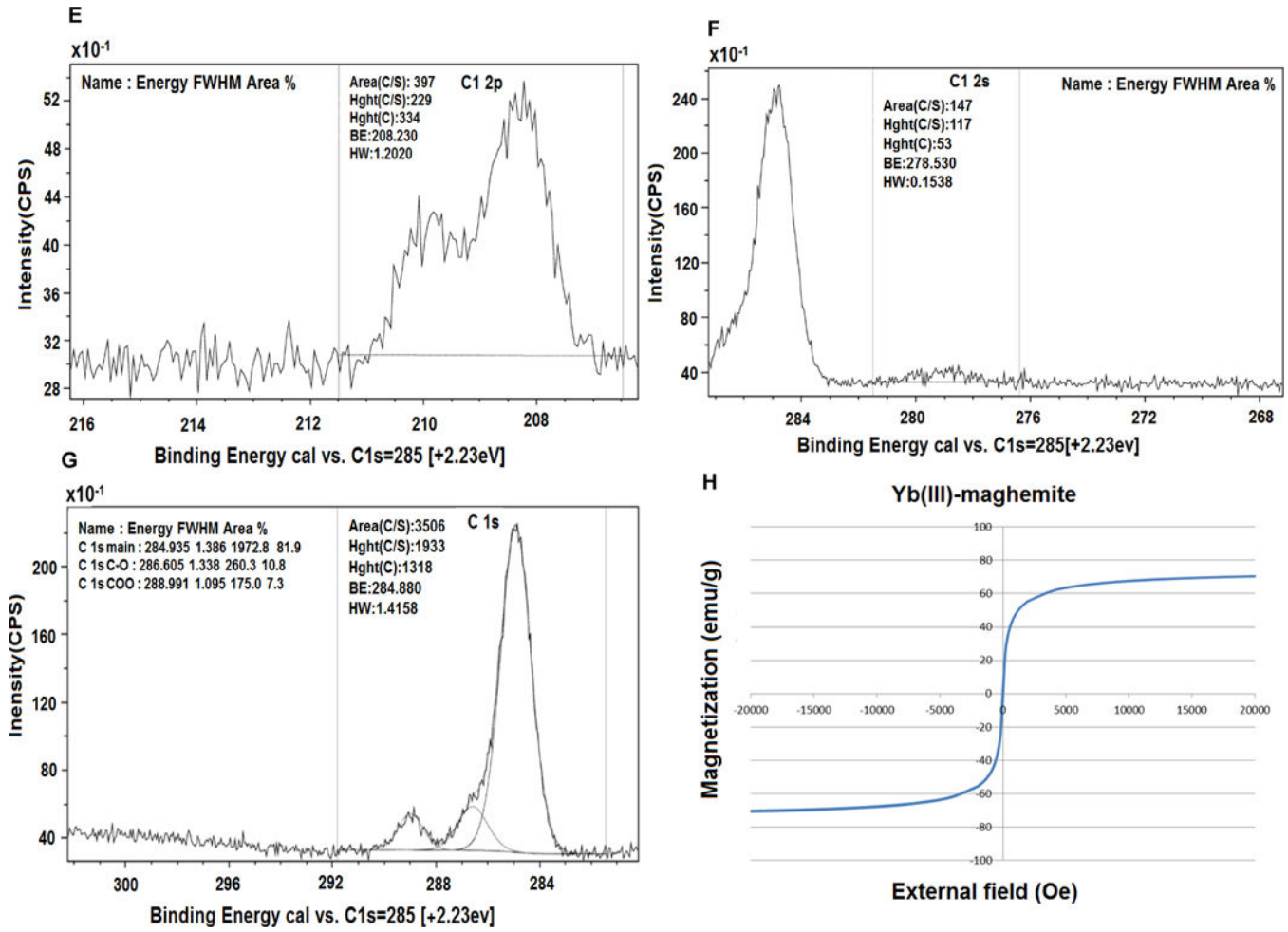

Figure 4. The core characterization of the Yb(III)-γ-Fe_2O_3 NPs

(**A**) TEM image, 50 nm scale bar. (**B**) SAED pattern analysis: (#1 (plane 220), #2 (plane 311), #3 (plane 400), & #6 (plane 440). (**C**) Size distribution by TEM (6.58 nm). (**D**) XRD analysis. XPS analysis: (**E)** C 1s area, (**F)**-Cl 2p area and (**G)** Cl 2s area. (H) SQUID magnetization profile (M*s* = 70.2 emu/g).

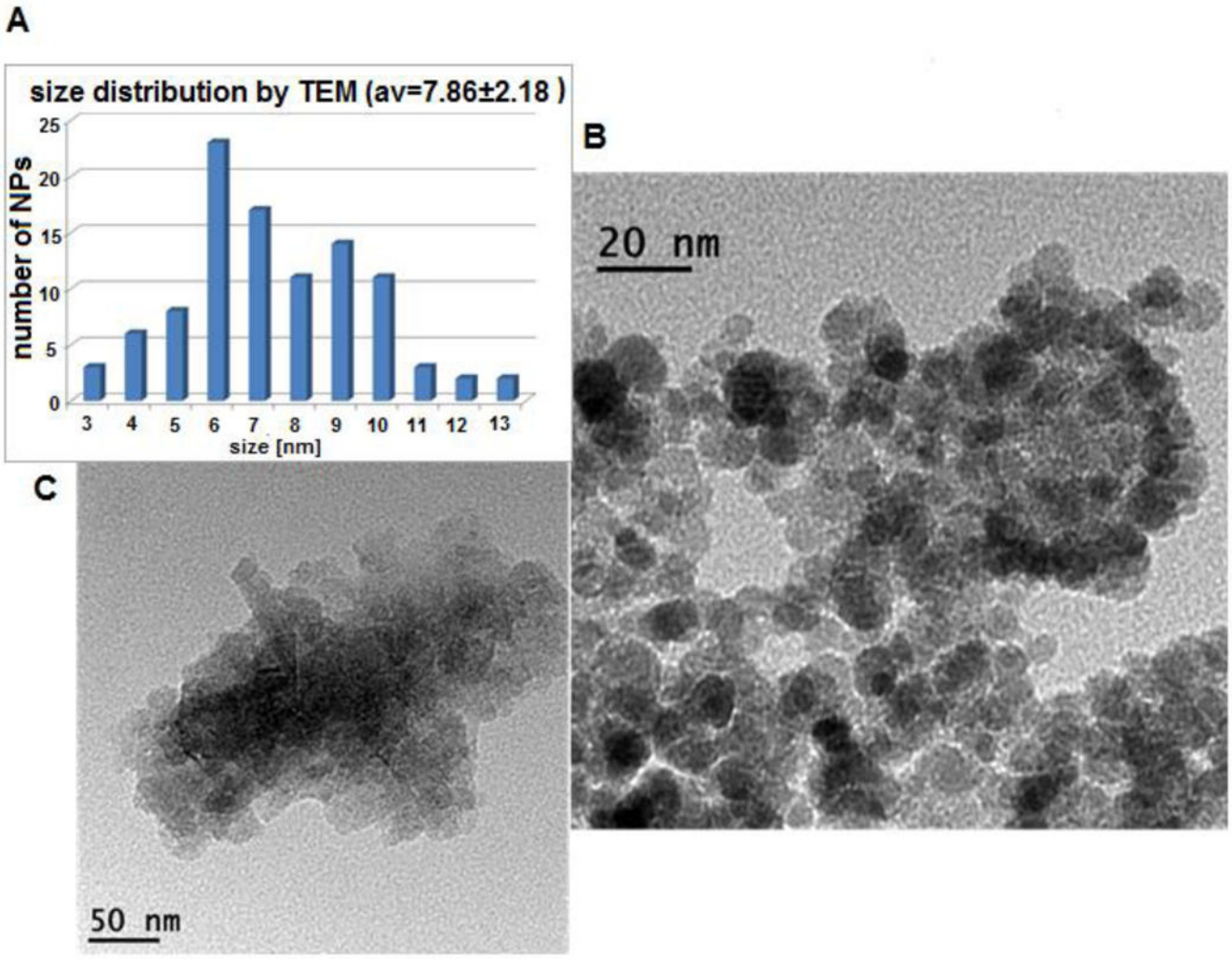

Figure 5. Yb(III)-γ-Fe2O3 NP size distribution

(A) NP size distribution by TEM (7.86±2.18 nm), and TEM images: **(B)** & **(**C**)** of HSA-28P.

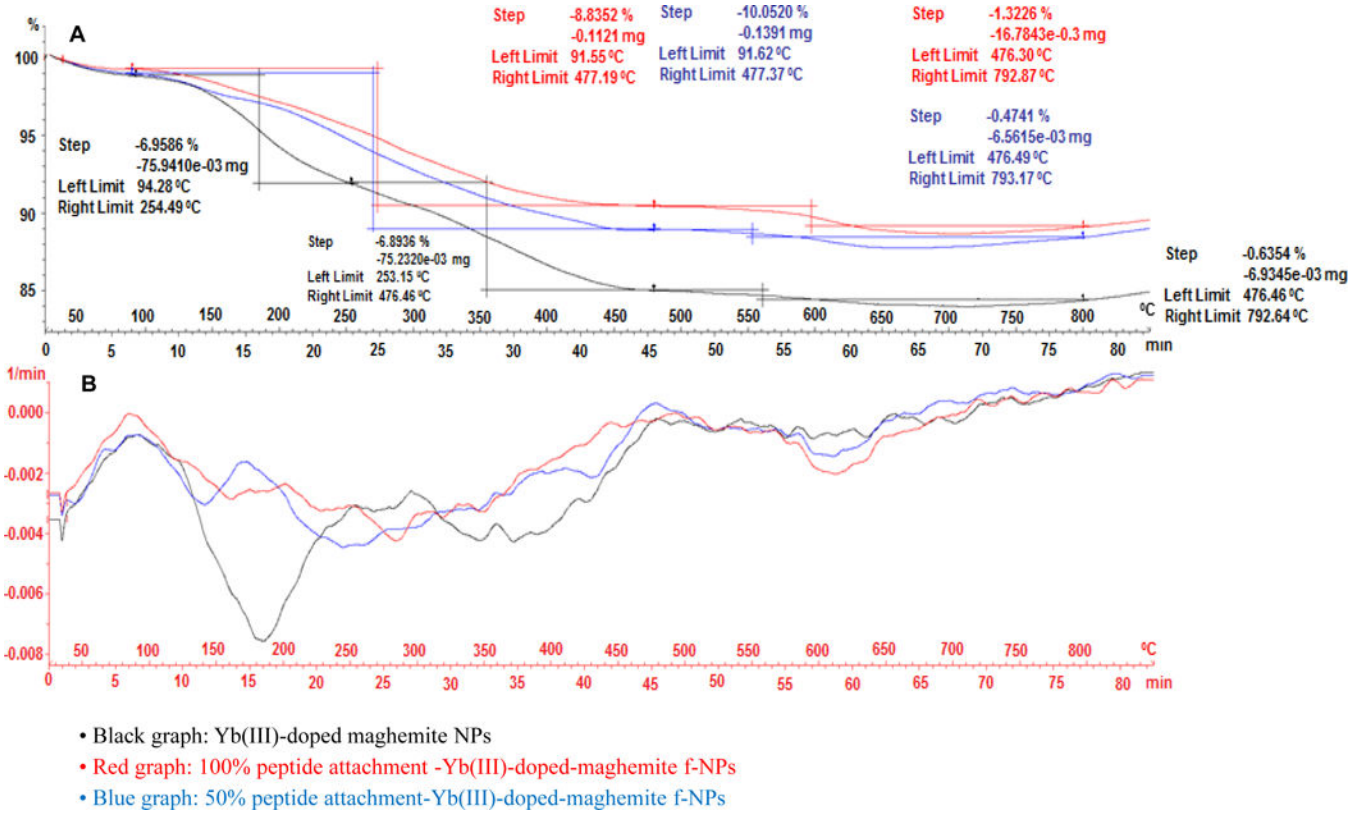

- Black graph: Yb(III)-doped maghemite NPs
- Red graph: 100% peptide attachment -Yb(III)-doped-maghemite f-NPs
- Blue graph: 50% peptide attachment-Yb(III)-doped-maghemite f-NPs

Figure 6. Thermogravimetric analysis of HSA-28P

TGA thermogram (**A**) and weight loss derivative function (**B**) graphs of Yb(III)-maghemite (black line), 100% peptide-Yb(III)-γ-Fe_2O_3 (red line), & 50% peptide-Yb(III)-γ-Fe_2O_3 NPs (blue line).

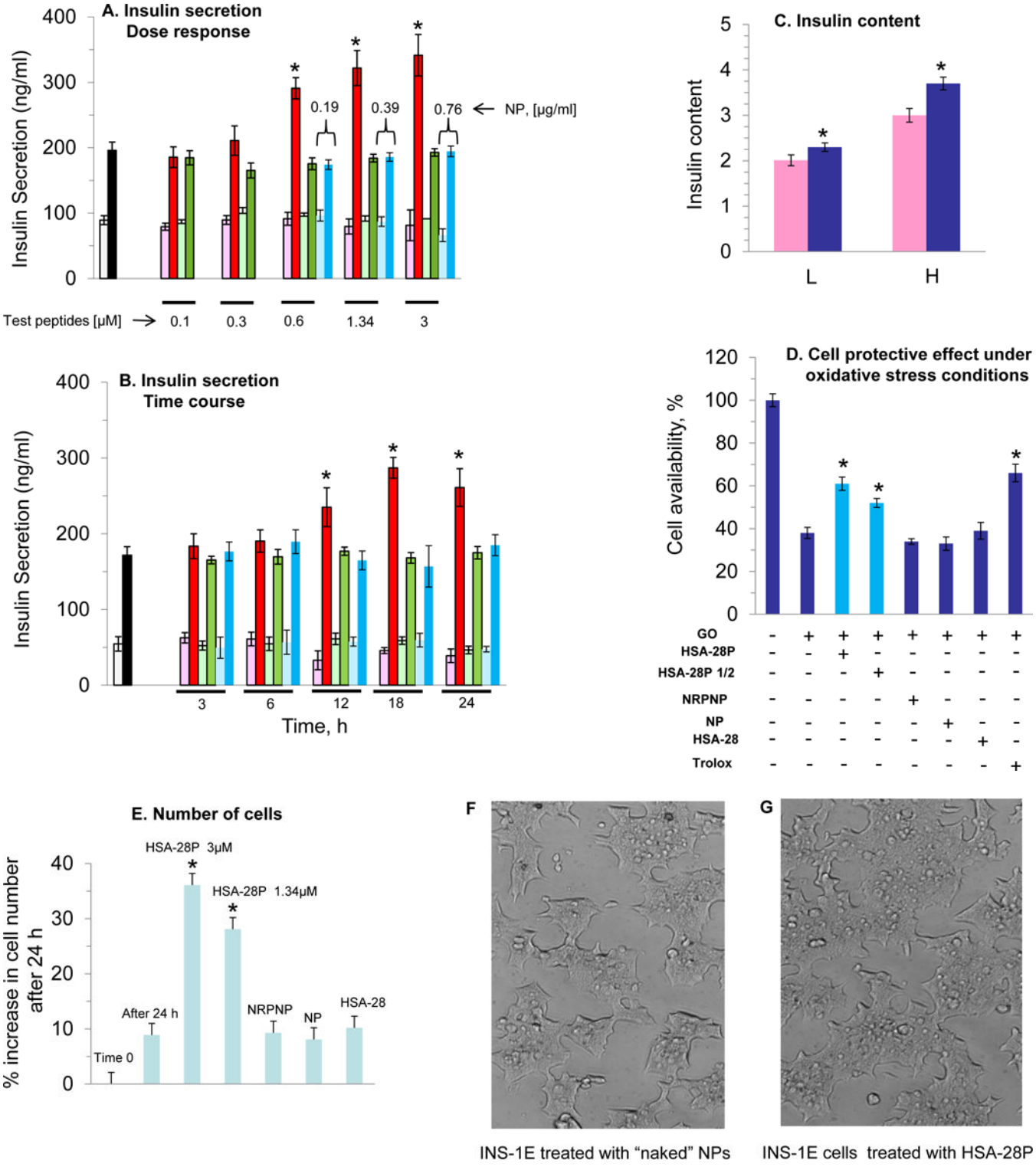

Figure 7. Evaluation of the biological activity of HSA-28P in INS-1E cells

A. Dose–response analysis of the effect of HSA-28P on the rate of insulin secretion in INS-1E cells. The INS-1E cells were grown and trypsinized as described in Methods. Subsequently, cells were mixed with the indicated concentrations of HSA-28P (red

columns), non-relevant peptide nanoparticles (NRPNP, green columns), and naked nanoparticles (NP, blue columns) and were seeded in 12-well plates. After 24 h the GSIS was analyzed in the presence of 2.5 mM (weak color bars) or 16.7 mM (strong color bars) glucose. **B**. Time-course analysis of the effect of HSA-28P on the rate of insulin secretion in INS-1E cells. The INS-1E cells were prepared for the experiment as described above with 1.34 μM of both HSA-28P or NRPNP, and 0.76 μg/ml of NP. After incubation for the time indicated in the graph, GSIS was measured described in Methods. **C**. *Measurement of insulin content.* The RIA-assay was performed for INS-1E lysates as previously described in Methods. **D.** The Effect of HSA-28P on the cells' viability under oxidative stress conditions. INS-1E cells were incubated for 24h with a medium supplemented with HSA-28P (3μM), or HSA-28P1/2 (1.5 μM), or NPs covered by phantom peptide (PPNP, 3μM), or NP (0.76 μg/ml), or HSA-28 (3μM) and trolox, as a positive antioxidant control (1 mM). After the incubation time, 50 mU/ml of glucose oxidase (GO) was added for an additional 1.15h. Upon completion of the experiments, a standard MTT assay was conducted as described in *Methods*. Cell viability is presented as a percentage in comparison to non-treated cells. **E.** *Effect of HSA-28P on the cell proliferation rate***.** Experiments were conducted on INS-1E cells that were seeded in 6-well plates. INS-1E cells were treated as described in Panel D. Cells were detached by trypsin and counted as described in Methods and then were visualized with a Cells Sense Live Imaging microscope. Panels **F**&**G** represent light microscope images of untreated cells and cells that were treated with HSA-28P, respectively. *$p<0.05$, n=3. MEAN±SE.

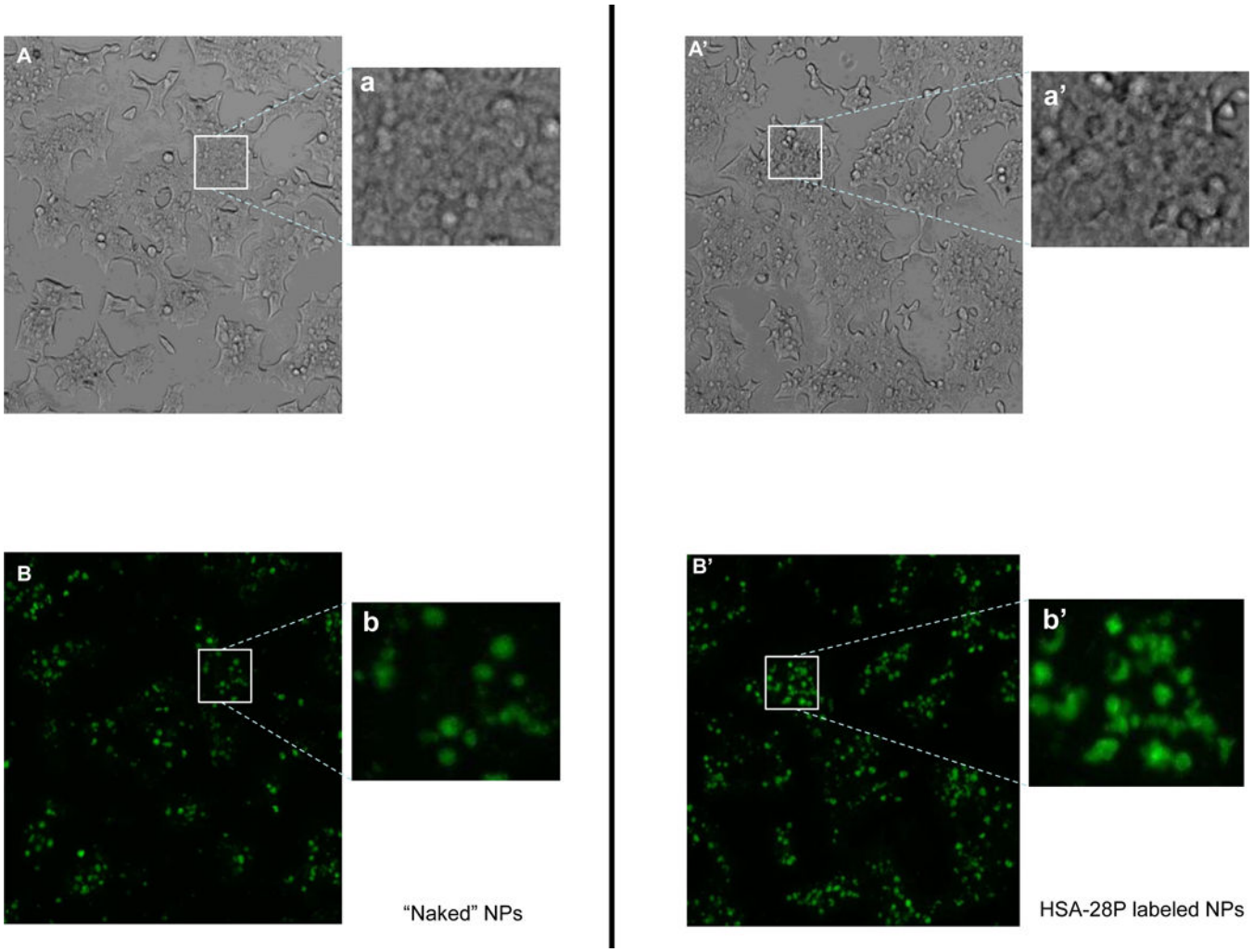

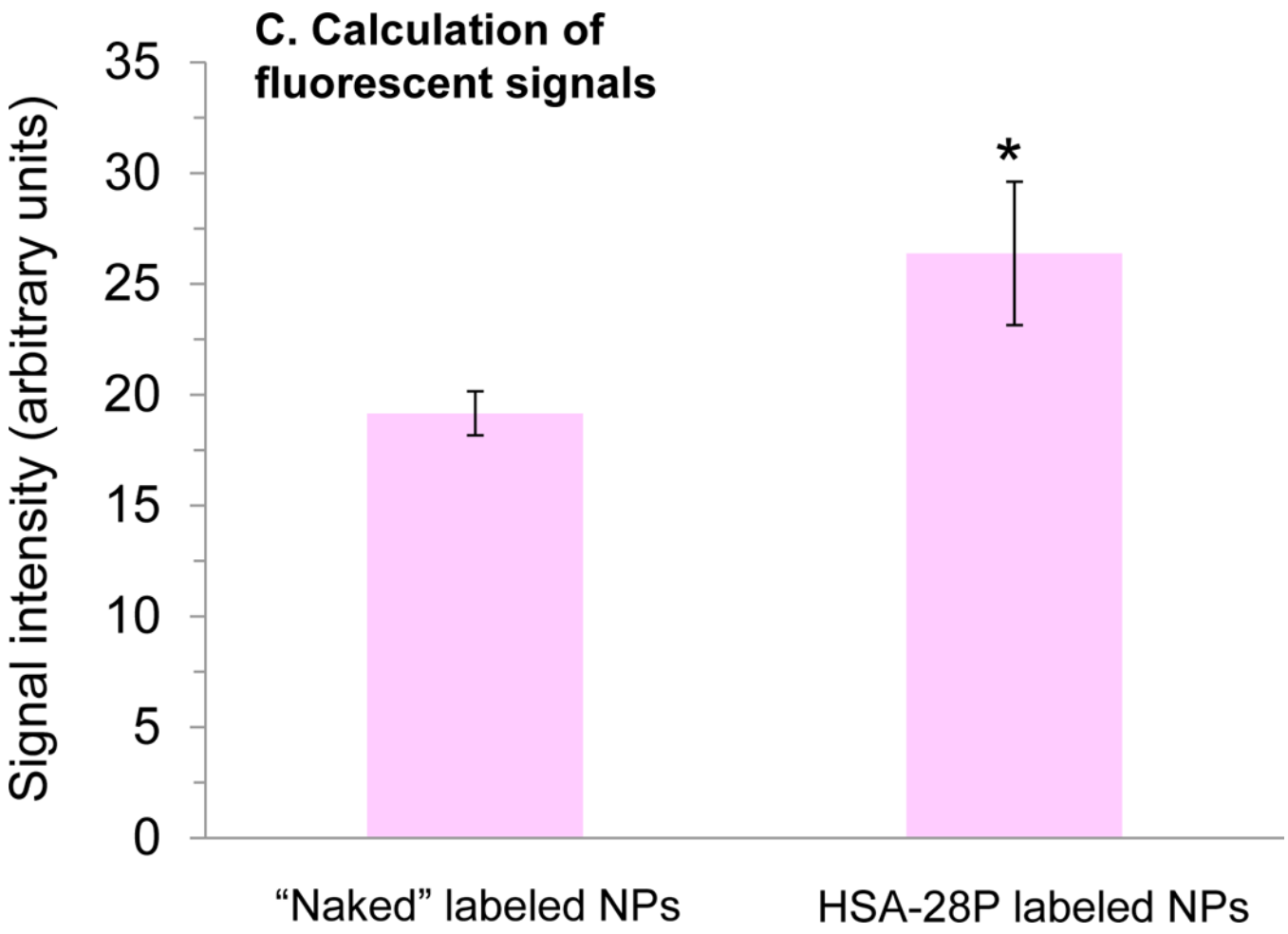

Figure 8. HSA-28P cell binding

Alive INS-1E cells were treated with "naked" NP (**A**) or with HSA-28P (**A**'), both NP were labeled by FITC as described above. The light microscope images were taken in different fields. Representative images are shown. In addition, corresponding close-up images (**a** and **a**`) are presented in the figure. An identical area was studied under a Cells Sense Live Imaging microscope and fluorescent images were taken in different fields. Representative images are shown. Treated by "naked" FITS-NP (**B**) and treated by FITS- HSA-28P (**B'**). The close-up images are also presented (**b** and **b**`, respectively). The quantitation results of the fluorescent green signal are presented in Panel **C**. The signal intensity was normalized by the number of cells. n=3,*p≤0.05, MEAN±SE.

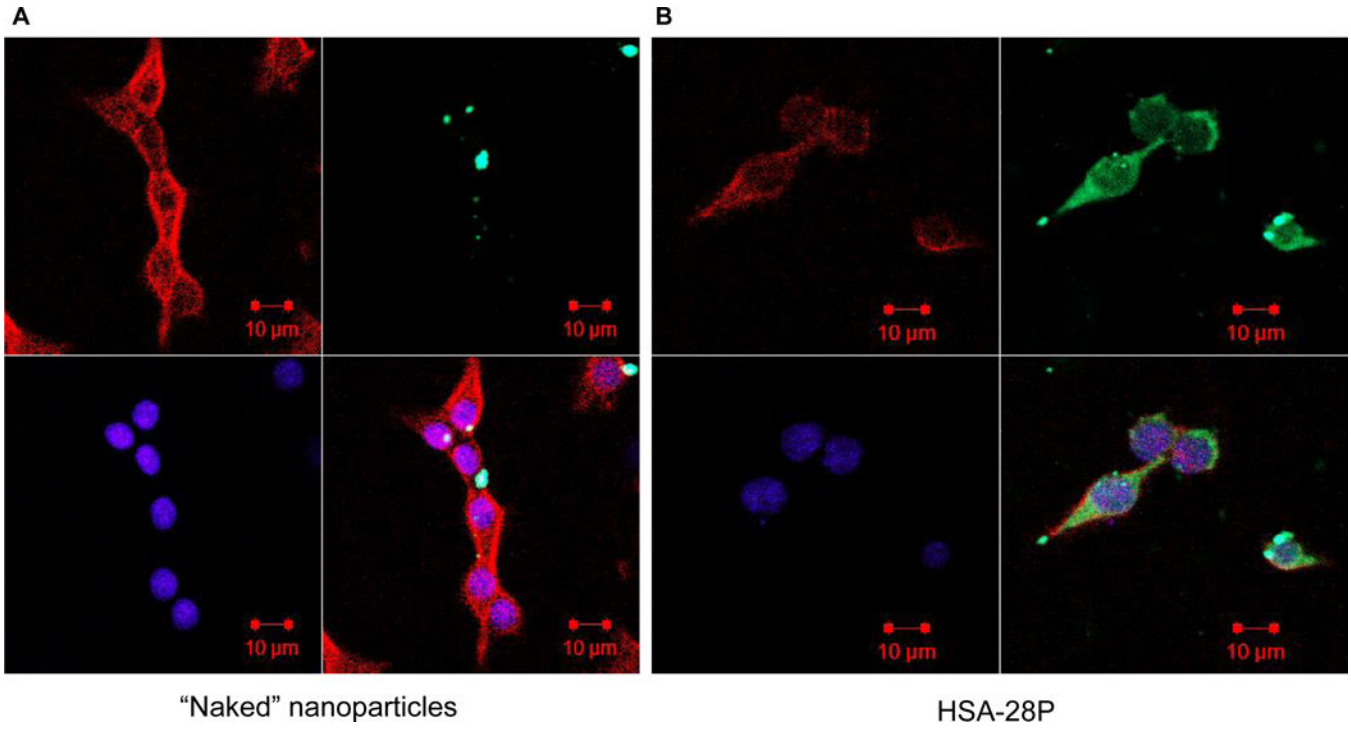

Figure 9. Cellular localization of HSA-28P

INS-1E cells were treated with FITC-labeled “naked” NP (green) (**A**) or with FITC-labeled HSA-28P (**B**) and then fixed as described in “*Methods*”. The obtained slides were stained with Alexa Fluor 633 Phalloidin for membrane (red) and with DAPI for nuclei (blue), as described in “Methods”. Cells were then visualized with a Confocal-Zeiss microscope. Representative images are shown. n=6.

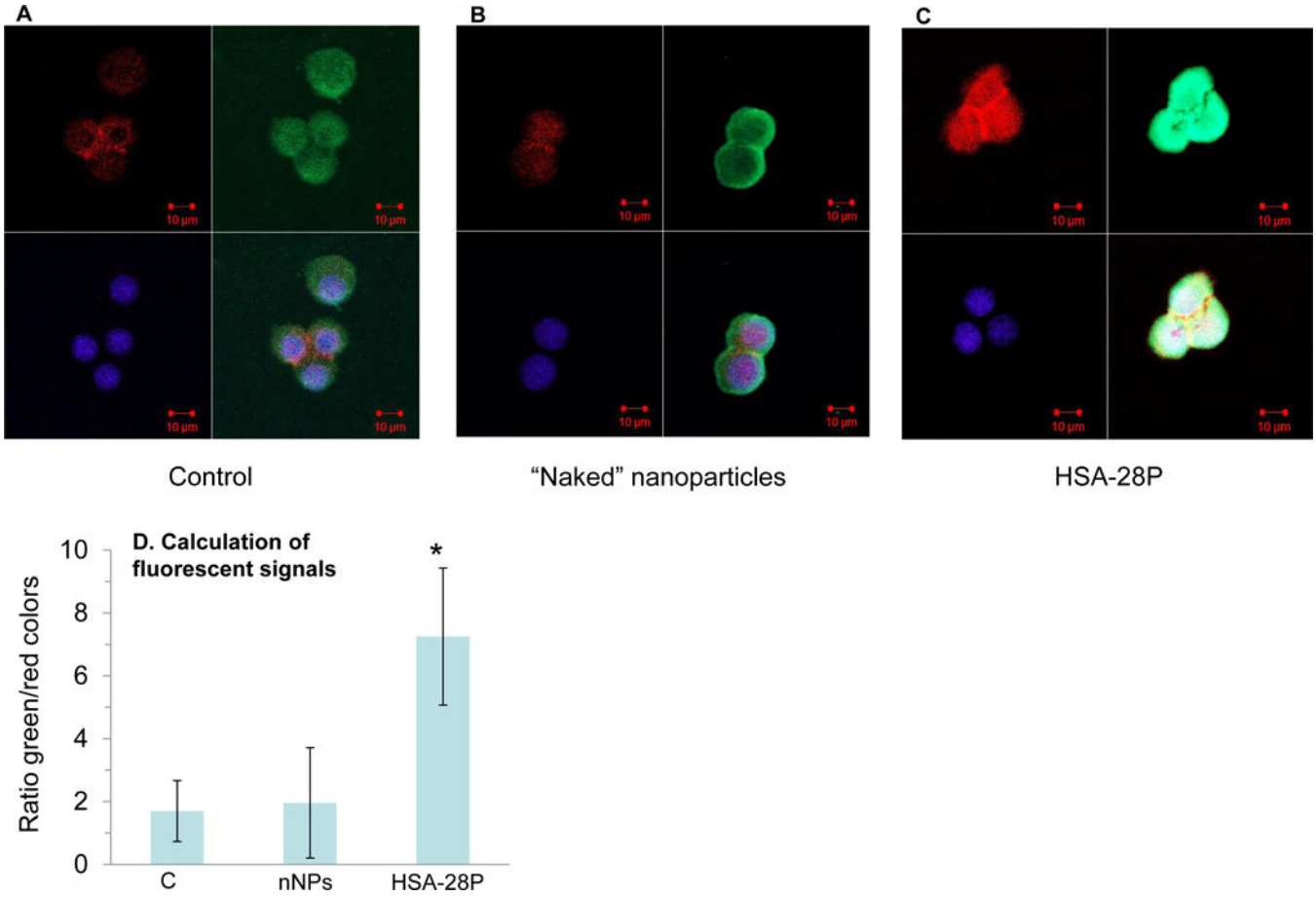

Figure 10. HSA-28P effect on C-peptide level

INS-1E cells (**A**) were treated with "naked" NP (**B**) or with HSA-28P (**C**) as described in "*Methods*". Cells were treated with antibody against C-peptide (green) according to the manufacturer's protocol and fixed. The obtained slides were stained with Alexa Fluor 633 Phalloidin for membrane (red) and with DAPI for nuclei (blue), as described in "Methods". Cells were then visualized with a Confocal-Zeiss microscope. The quantitation results of the C-peptide signal are presented in Panel **D**. The signal intensity was normalized by the total intensity of the membrane signal. Representative images are shown. n=12. *p≤0.05, MEAN ±SE.

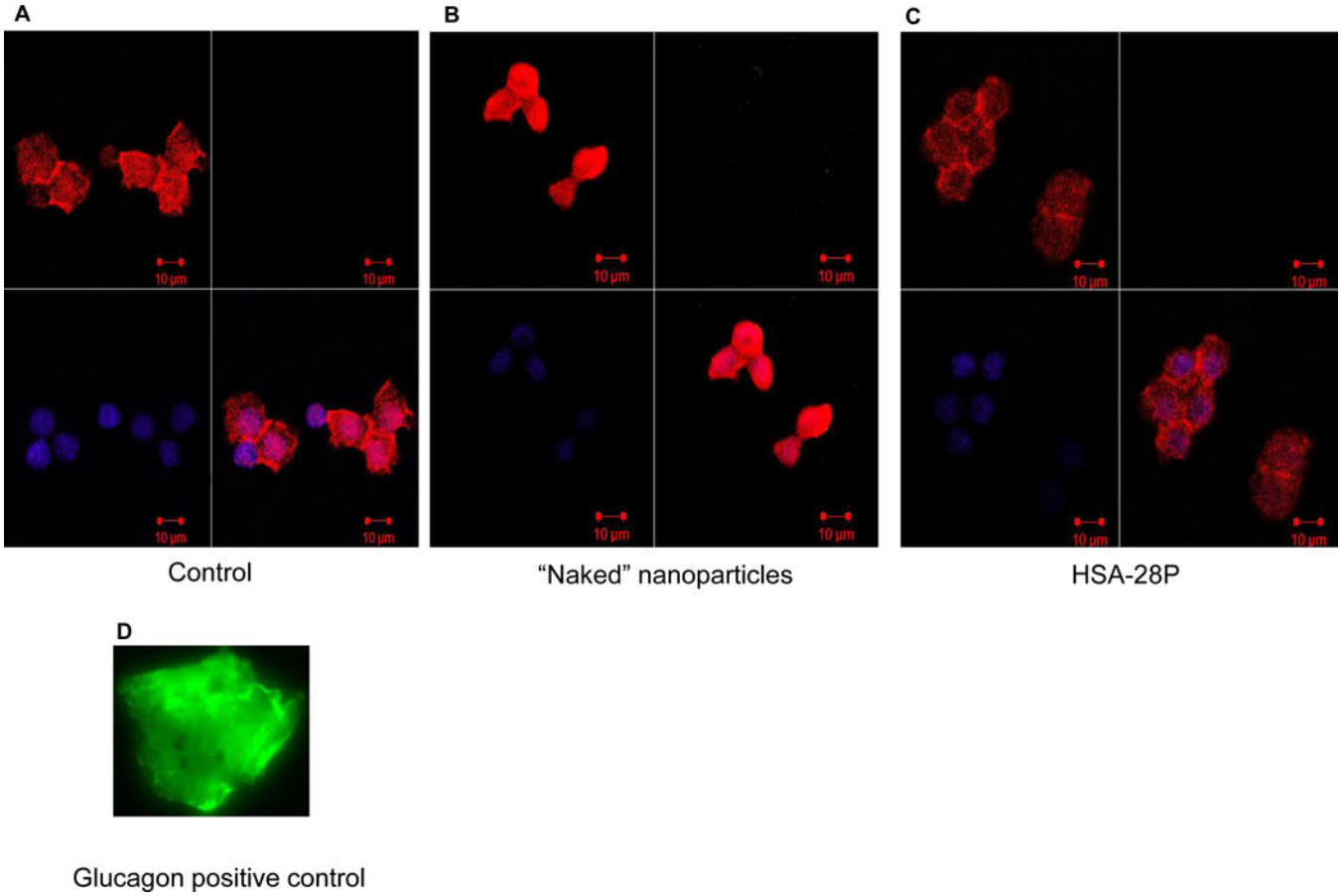

Figure 11. Cell proliferation effect of HSA-28P does not induce glucagon synthesis

INS-1E cells (**A**) were treated with "naked" NP (**B**) or with HSA-28P (**C**) as described in "*Methods*". Cells were treated with antibody against glucagon (green) (**D**) according to the manufacturer's protocol and fixed. The obtained slides were stained with Alexa Fluor 633 Phalloidin for membrane (red) and with DAPI for nuclei (blue), as described in "Methods". Cells were then visualized with a Confocal-Zeiss microscope. The signal intensity was normalized by the total intensity of the membrane signal. Representative images are shown. n=6.

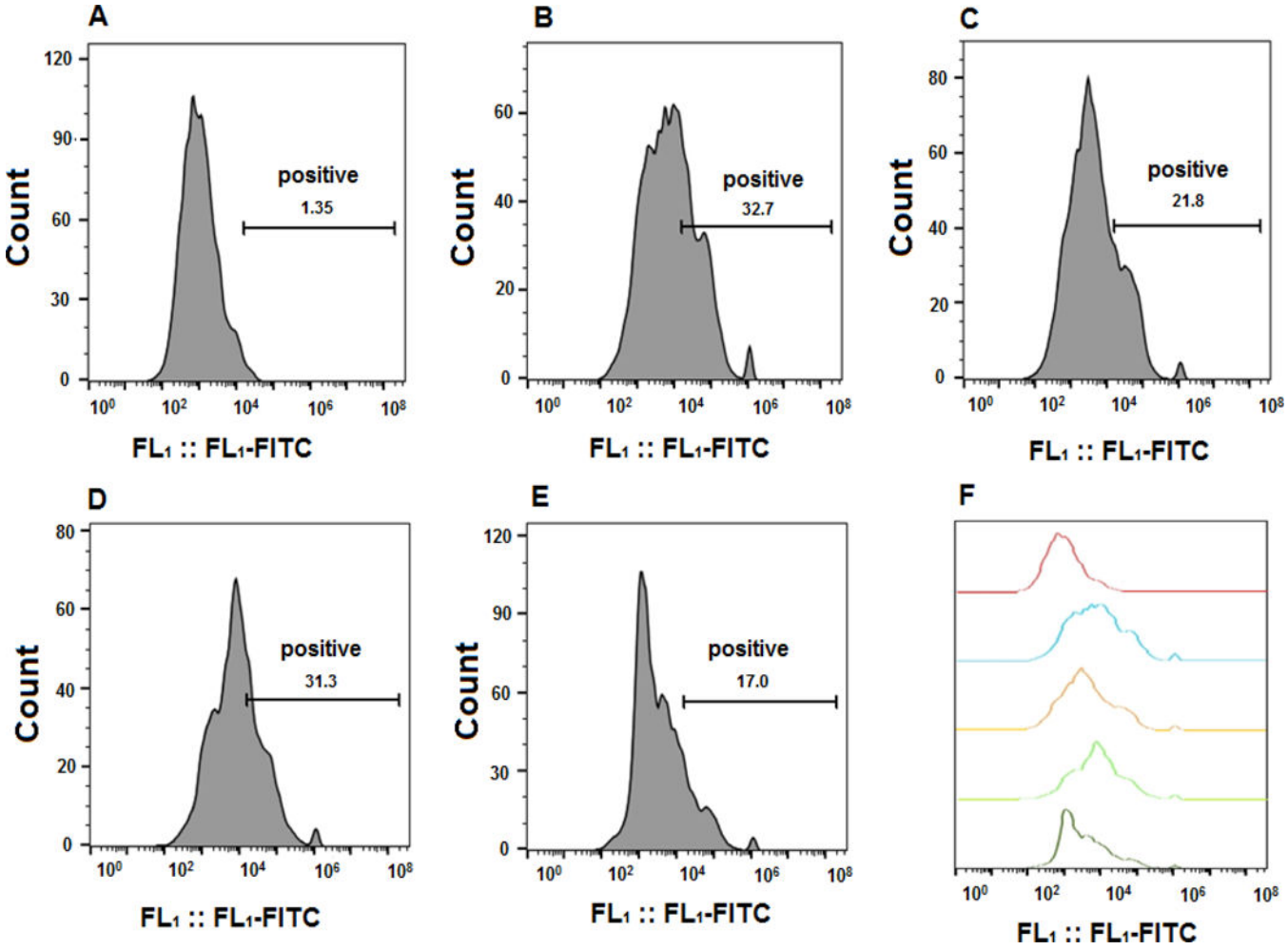

	Sample name	Subset Name	Count	Geometric Mean : FL1-A	% difference in signal intensity
	01-neg-2016-11-09-133729-1.fcs	cells	3693	1015	-
	02-cont-2016-11-09-13524.fcs	cells	3631	7743	0
	03-treat. By HSA-28P-2016-11-09-134020-3.fcs	cells	3727	4342	-44
	04-treat. by nNP-2016-11-09-134742-4.fcs	cells	2833	8205	+5
	05-treat. by HSA-28-2016-11-09-134902-5.fcs	cells	3677	3710	-52

Figure 12. Effect of HSA-28P and HSA-28 on the binding affinity of anti-Neurexin 1α antibody

INS-1E cells that were seeded in 12-well plates. The cells were incubated with HSA-28P, “naked” nanoparticles or HSA-28 peptide for 24 h. After the indicated incubation time, cells were exposed to ATTO 488-fluorescent labeled antibody against an extracellular epitope of Neurexin 1α according to the manufacturer`s protocol. After then, cells were taken to Gallios Fluorescence Activated Cell Sorter. Control cells (A), treated only by anti-Neurexin 1α antibody (**B**), treated by HSA-28P and anti-Neurexin 1α antibody (**C**), treated by

"naked" nanoparticles and anti-Neurexin 1α antibody (**D**) and finally cells treated by HSA-28 and anti-Neurexin 1α antibody (**E**). The summary of the spectra of the fluorescent signals (F). The summary of cell counts and percentage of the inhibition. n=3.

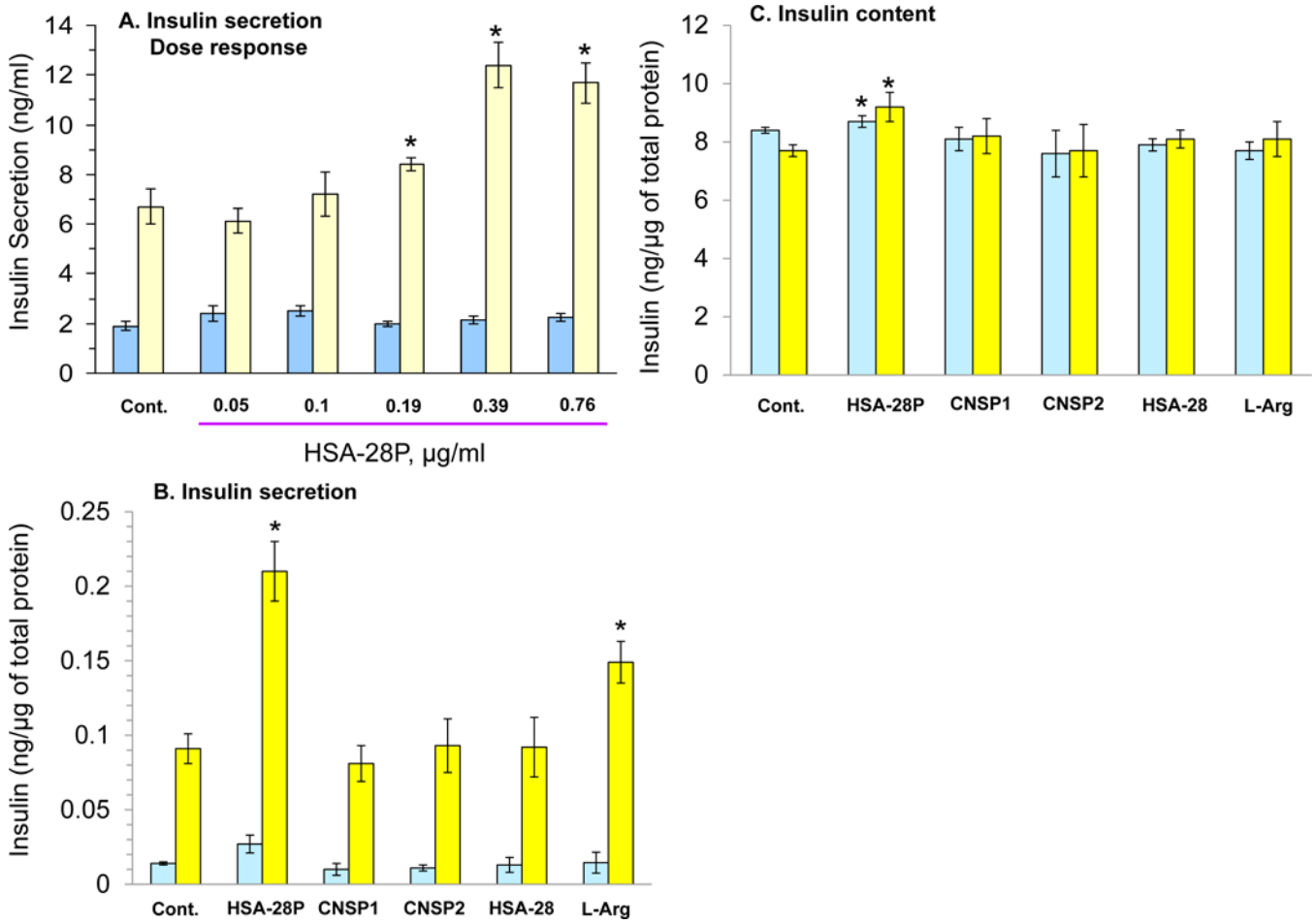

Figure 13. Effect of HSA-28P on insulin secretion in mouse islets

A. Dose–response analysis of the effect of HSA-28P on the rate of insulin secretion in isolated mouse islets. Islets were isolated and treated as described in Methods. Subsequently, HSA-28P was added to islets at the indicated concentrations. After 24 h islet GSIS was analyzed in the presence of 2.5 mM (blue bars) or 16.7 mM (yellow bars) glucose. **B**. Effect of HSA-28P on the rate of insulin secretion compared to the control treatments in mouse islets. Mouse islets were prepared for the experiment as described in Panel A. Briefly, 0.76 µg/ml of HSA-28P or HSA-28, or CNSP1, or CNSP2, or L-arginine (L-Arg) was added for 24 h. Thereafter, islets were taken to a GSIS as described in Methods. **C**. *Measurement of insulin content.* Islets were treated as described in Panel B. The RIA-assay was performed for INS-1E lysates as previously described in Methods. *p<0.05, n=3. MEAN±SE.

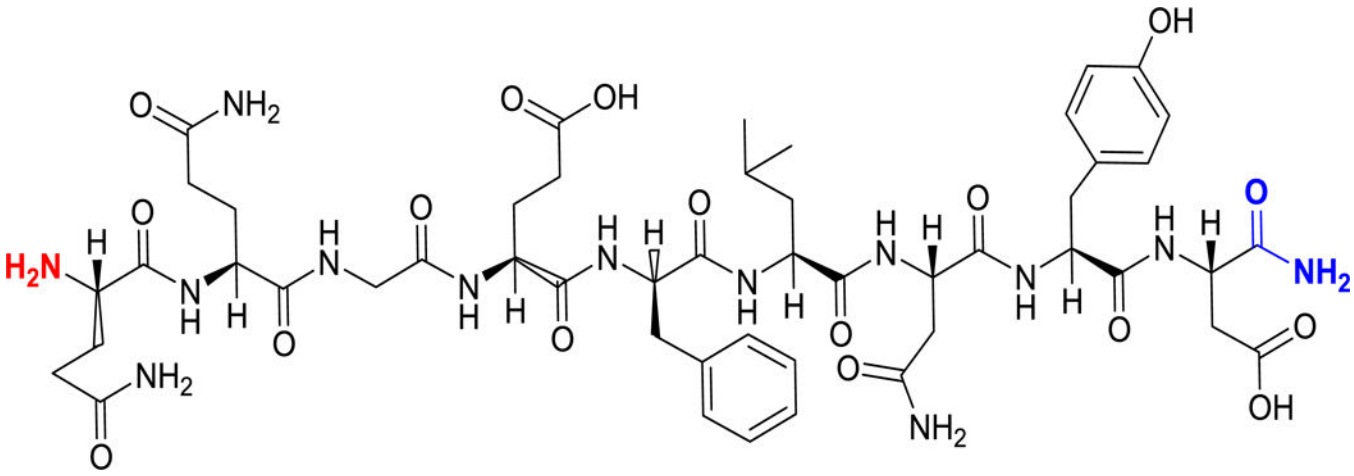

Chart 1.
Chemical structure of the HSA-28 peptide derived from the NL-4/NX-1 complex

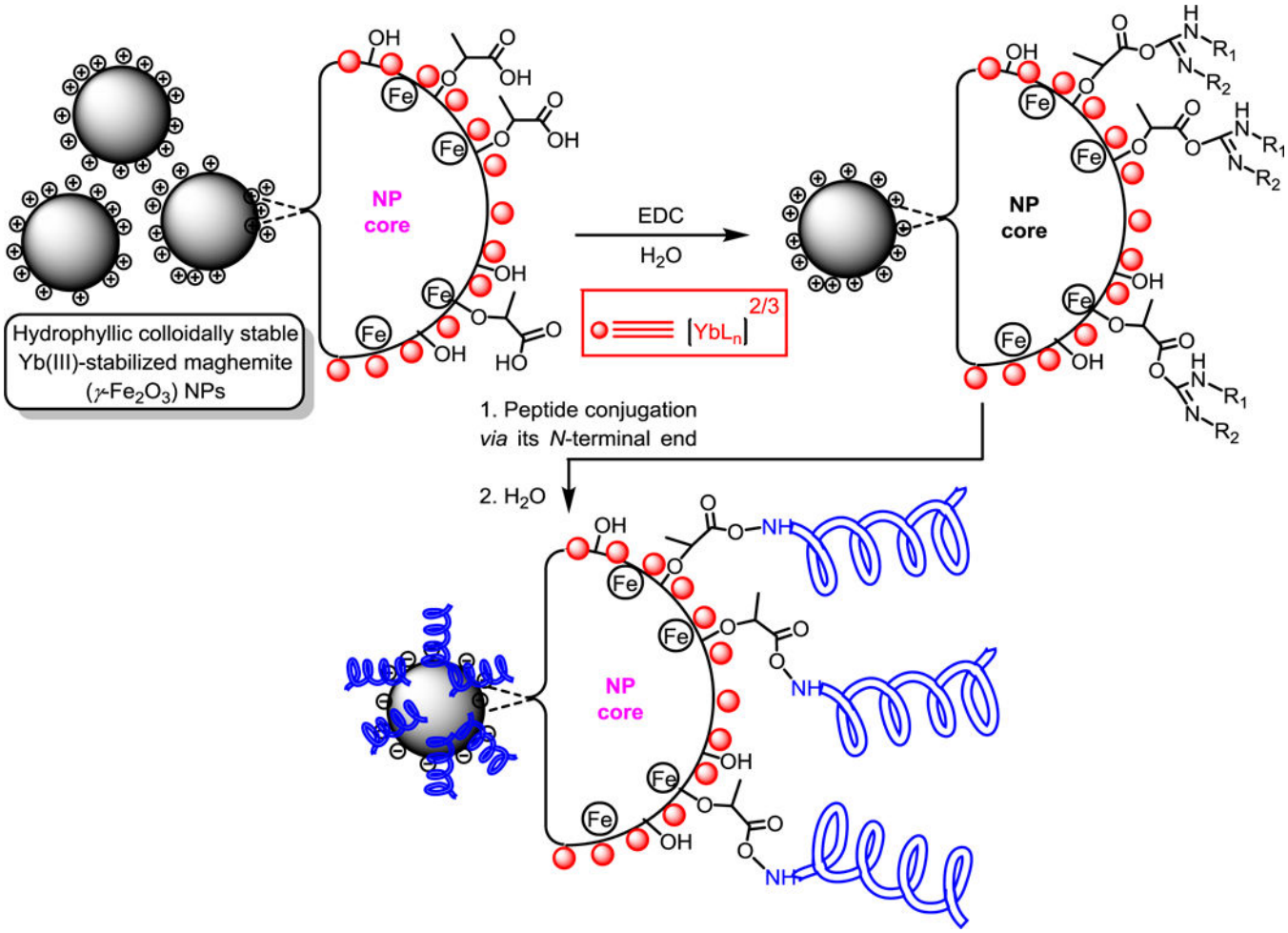

Scheme 1.
Preparation of HSA-28P

Table 1.

NP	Mean hydrodynamic diameter by DLS [nm]	Size by TEM [nm]	Zeta potential [mV]	Fe [mg/mL] using ICP or AAS	Doping metal [mg/mL] using ICP or AAS	Doping metal to Fe Wt ratio	Doping metal to Fe Molar ratio
Yb(III) cation-doped maghemite NPs	42	6.58 ± 2.03	(+)46 (+)50	1.476	0.272	0.184	0.059